Key factors determining nightside energetic electron losses driven by whistler-mode waves

Ethan Tsai [1], Anton Artemyev [1], Qianli Ma [2,3], Didier Mourenas [4,5], Oleksiy Agapitov [6], Xiao-Jia Zhang [7,1], Vassilis Angelopoulos [1]

[1]Earth, Planetary, and Space Sciences, University of California, Los Angeles, Los Angeles, CA 90095, USA
[2]Department of Atmospheric and Oceanic Sciences, University of California, Los Angeles, Los Angeles, USA
[3]Boston University, Boston, MA, United States
[4]CEA, DAM, DIF, Arpajon, France
[5]Laboratoire Matière en Conditions Extrêmes, Paris-Saclay University, CEA, Bruyères-le-Châtel, France
[6]Space Sciences Laboratory, University of California, Berkeley, CA, USA
[7]Department of Physics, The University of Texas at Dallas, Richardson, TX, USA

Key Points:

- Comparing ELFIN data with test particle and quasi-linear simulations, we investigate whistler-driven electron precipitation on the nightside
- A reduction in background plasma density is key to enabling whistler-mode waves to efficiently scatter electrons up to 1 MeV
- Decreasing wave frequency as a function of latitude and wave obliquity, are both integral to capturing realistic nightside electron losses

Corresponding author: Ethan Tsai, ethantsai@ucla.edu

Abstract

Energetic electron losses by pitch-angle scattering and precipitation to the atmosphere from the radiation belts are controlled, to a great extent, by resonant wave particle interactions with whistler-mode waves. The efficacy of such precipitation is primarily controlled by wave intensity, although its relative importance, compared to other wave and plasma parameters, remains unclear. Precipitation spectra from the low-altitude, polar-orbiting ELFIN mission have previously been demonstrated to be consistent with energetic precipitation modeling derived from empirical models of field-aligned wave power across a wide-swath of local-time sectors. However, such modeling could not explain the intense, relativistic electron precipitation observed on the nightside. Therefore, this study aims to additionally consider the contributions of three modifications – wave obliquity, frequency spectrum, and local plasma density – to explain this discrepancy on the nightside. By incorporating these effects into both test particle simulations and quasi-linear diffusion modeling, we find that realistic implementations of each individual modification result in only slight changes to the electron precipitation spectrum. However, these modifications, when combined, enable more accurate modeling of ELFIN-observed spectra. In particular, a significant reduction in plasma density enables lower frequency waves, oblique, or even quasi-field aligned waves to resonate with near ~ 1 MeV electrons closer to the equator. We demonstrate that the levels of modification required to accurately reproduce the nightside spectra of whistler-mode wave-driven relativistic electron precipitation match empirical expectations, and should therefore be included in future radiation belt modeling.

Plain Language Summary

Whistler-mode waves are a type of electromagnetic wave that mediate electron dynamics in Earth's radiation belts and are simultaneously important for energizing electrons and driving loss mechanisms. Most radiation belt models today do not adequately capture the effects of these waves on relativistic electrons, which are important to study because these energetic electrons are often called "Killer Electrons" for their ability to degrade spacecraft electronics. Additionally, when lost into Earth's atmosphere, these electrons can also change atmospheric chemistry and ionospheric properties, making them an important input parameters for atmospheric, ionospheric, and magnetospheric modeling. This study uses two different modeling methods to determine which properties of whistler-mode waves are most important for accurately capturing these wave-particle interactions on the nightside, where plasma interactions are more dynamic. The results agree well with statistical results from the Electron Losses and Fields INvestigation (ELFIN) mission, allowing us to fully explain the mechanisms behind whistler-mode wave-driven electron losses on the nightside.

1 Introduction

Earth's inner magnetosphere is filled with energetic electron fluxes injected from the plasma sheet, that are then further accelerated via resonant interactions with electromagnetic whistler-mode (chorus) waves (Millan & Baker, 2012; Shprits et al., 2008). These wave-particle interactions are, in great part, also responsible for energetic electron pitch-angle scattering into the loss cone and subsequent electron loss through precipitation into Earth's atmosphere (Millan & Thorne, 2007; Shprits et al., 2008). This contribution to both acceleration and pitch-angle scattering of energetic electrons makes the whistler-mode wave a crucial element of outer radiation belt dynamics (Bortnik & Thorne, 2007; Thorne, 2010; Li & Hudson, 2019). Not only do energetic radiation belt electrons serve as an important space weather proxy (Horne et al., 2013), relativistic electron can also penetrate deep into the thermosphere/mesosphere (Xu et al., 2020) contributing to ozone depletion (Thorne, 1980; Lam et al., 2010; Turunen et al., 2016). Un-

derstanding the mechanisms behind the global distribution of energetic electron losses is therefore important for studying radiation belt dynamics and atmospheric chemistry.

Energetic ($\gtrsim$ 100 keV) electron losses due to whistler-mode waves is one such topic that has yet to be fully investigated. It is known that these waves can scatter electrons up to 1 MeV (O'Brien et al., 2004; Thorne et al., 2005; Blake & O'Brien, 2016; Shumko et al., 2018; Breneman et al., 2017), which is problematic because current radiation belt models typically only incorporate diffusive losses of sub-relativistic electrons (up to $\sim$ 500 keV). Additionally, previous research (Tsai et al., 2023) has revealed a day-night difference in energetic electrons scattered by whistler-mode waves, with more intense electron precipitation on the dayside than on the nightside. This is attributed to two system-level properties – (1) nightside regions generally have a lower plasma density and (2) nightside wave activity is generally more confined to the equatorial plane (Meredith et al., 2001, 2003; Agapitov et al., 2013) – which both cause strong resonant wave particle interactions to preferentially occur on the dayside, resulting in more extreme energetic electron losses (e.g., Thorne et al., 2005; Mourenas, Artemyev, Agapitov, & Krasnoselskikh, 2014; Wang & Shprits, 2019; Aryan et al., 2020). This is supported by Tsai et al. (2023), which used modeled electron precipitation spectra derived from statistically-averaged wave intensity distributions from Agapitov et al. (2018) to directly compare with statistical observations of electron precipitating fluxes from ELFIN (Angelopoulos et al., 2020). Although these model-data comparisons showed good agreement between electron precipitation and wave power in the dusk and daysides, ELFIN-measured nightside relativistic ($\gtrsim$ 500 keV) precipitating flux rates were substantially larger than anticipated (i.e. modeled) and nearly comparable to that on the dayside. Understanding mechanisms that can cause such intense energetic precipitation is a prerequisite for accurately modeling electron loss in the radiation belts, therefore motivating the need to explore what key factors actually determine nightside electron losses.

There are a few prime candidates that determine the efficiency of wave-particle resonant interactions (and, particularly, the energy dependence of whistler-mode wave driven electron scattering):

1. Wave intensity distribution along magnetic field lines (see discussion in Thorne et al., 2005; Wang & Shprits, 2019).
2. Obliquity of wave propagation relative to the background magnetic field (see discussion in Lorentzen et al., 2001; Mourenas, Artemyev, Agapitov, & Krasnoselskikh, 2014; Artemyev et al., 2016).
3. Wave frequency spectrum and its variation along magnetic field lines (see discussion in Agapitov et al., 2018)
4. Equatorial plasma density magnitude (see discussion in Thorne et al., 2013; Agapitov et al., 2019; Allison & Shprits, 2020) and its variation along magnetic field lines (see discussion in Summers & Ni, 2008; Artemyev et al., 2013).

Having already examined the importance of wave amplitude in Tsai et al. (2023), we now study the remaining three mechanisms which could potentially modulate nightside electron precipitating spectra. First, intense nightside whistler-mode waves are typically associated with strong plasma sheet injections (Tao et al., 2011; Fu et al., 2014; X. Zhang et al., 2018) which are often accompanied by the enhanced convection electric field which transports cold plasma Earthward, thereby decreasing equatorial plasma density (Vasko, Agapitov, Mozer, Bonnell, et al., 2017; Agapitov et al., 2019). A lower plasma density results in a lower plasma frequency; a lower plasma frequency to gyrofrequency ratio, f_{pe}/f_{ce} yields a higher cyclotron resonance energy $E_R \propto (f_{ce}/f_{pe})^2$ to f_{ce}/f_{pe} (from low to high energy) of electrons for given wave frequencies, wave normal angles, and electron pitch-angles (Stix, 1962; Summers et al., 2007; Li, Thorne, Nishimura, et al., 2010; Allison et al., 2021). This nightside localized density reduction can thus potentially increase the scattering rate of relativistic electrons.

Second, statistical observations have shown a clear trend of average wave frequency decreasing with latitude along field lines (i.e. increasing distance from the equatorial plane) (Agapitov et al., 2018). This is likely caused by preferential Landau damping of higher-frequency waves resonating with suprathermal electrons (L. Chen et al., 2013; Watt et al., 2013; Maxworth & Golkowski, 2017). A lower normalized wave frequency f/f_{ce} means a higher cyclotron resonance energy $E_R \propto (f_{ce}/f)(1-f/f_{ce})^3$ to $(f_{ce}/f)^{1/2}(1-f/f_{ce})^{3/2}$ from low to high energy (Li, Thorne, Nishimura, et al., 2010; Mourenas et al., 2012). Thus, this reduction in the mean wave frequency in the nightside off-equatorial region may also increase the scattering rate of relativistic electrons.

Third, plasma injections are often associated with enhanced electrostatic turbulence (Mozer et al., 2015; Agapitov et al., 2015; Vasko, Agapitov, Mozer, Artemyev, et al., 2017; Malaspina et al., 2018) that forms a plateau in the field-aligned velocity distribution and significantly reduces Landau damping of oblique whistler-mode waves (see discussion in Mourenas et al., 2015; Ma et al., 2017; Artemyev & Mourenas, 2020). In this regime, oblique (with wave normal angles below the Gendrin angle $\theta_G \approx \mathrm{acos}(2f/f_{ce})$) and very oblique (with wave normal angle up to the resonant cone angle $\theta_r \approx \mathrm{acos}(f/f_{ce})$) waves may survive Landau damping (see Min et al., 2014; R. Chen et al., 2019; Sauer et al., 2020; Ke et al., 2022). These waves then become oblique off the equatorial plane (Bortnik et al., 2007; L. Chen et al., 2013), or, in more unusual cases, are generated within the equatorial source region (Artemyev et al., 2016; Li, Mourenas, et al., 2016; Agapitov et al., 2016). Wave obliquity not only increases the resonant interaction energy with electrons as $E_R \propto 1/k_\parallel^2 \propto 1/\cos^2\theta$ (e.g., Verkhoglyadova et al., 2010; Mourenas et al., 2015), but also allows for interactions with electrons at higher-order cyclotron resonances ($n \gg 1$, e.g., Shklyar & Matsumoto, 2009; Mourenas et al., 2012; Artemyev et al., 2013; Albert, 2017) which can drastically increase the resonance energy $E_R \propto n^2$ (e.g., Lorentzen et al., 2001; Gan et al., 2023). Thus, nightside whistler-mode wave obliquity could also potentially increase the scattering rate of relativistic electrons.

Here, we examine each of these three mechanisms to see whether they can explain the enhanced precipitation of relativistic electrons in the nightside MLT sector using a combination of statistics from ELFIN observations (Angelopoulos et al., 2020), test particle simulations (Tsai et al., 2022, 2023), and quasi-linear diffusion code (Ma et al., 2012, 2015). This paper is organized as follows: Section 2 details ELFIN observations/statistics and presents observational evidence of intense nightside precipitation of relativistic electrons; Section 3 describes the basics of the test particle simulation and quasi-linear diffusion codes; Section 4 compares ELFIN data to results from a variety of runs exploring the three main modifications – reduced plasma density, wave obliquity, wave frequency variation along magnetic field lines; finally, Section 5 summarizes and discusses the obtained results.

2 Data Sets

The ELFIN CubeSats (ELFIN A and B) are identically equipped with an Energetic Particle Detector for Electrons (EPDE), capable of measuring energy and pitch-angle distributions of energetic electrons with $\Delta E/E = 40\%$ across 16 logarithmically spaced energy channels between 50 keV and 5 MeV (Angelopoulos et al., 2020). Spinning at just over 21 revolutions per minute (spin period ≈ 2.8 sec), ELFIN's 16 sectors per spin yields a spin phase resolution of $\Delta\alpha = 22.5°$. The main data product used in this study is the precipitating-to-trapped flux ratio, $j_{prec}/j_{trap}(E)$, where $j_{trap}(E)$ is the locally trapped (outside of the local bounce loss-cone) electron flux and $j_{prec}(E)$ is the flux integrated over the local loss-cone with a correction to remove the backscattered fluxes from the opposite hemisphere (see details in Mourenas et al., 2021; Angelopoulos et al., 2023). Figure 1 shows two typical examples of ELFIN outer radiation belt crossings on the nightside with $j_{trap}(E)$ (a,d) and j_{prec}/j_{trap} (b,e) distributions.

This study utilized 30 months (January 2020 - June 2022) of ELFIN's $j_{trap}(E)$ and $j_{prec}(E)$ measurements during strong and bursty energetic electron precipitation events (for details regarding statistical coverage, see Figure 5 in Tsai et al., 2023). In order to obtain a statistical representation of whistler-mode-driven electron precipitation, data was selected based on data quality (minimum 4 counts/second for any given energy or pitch angle bin) and precipitation intensity ($j_{prec}(E)/j_{trap}(E) > 0.5$ at ELFIN's lowest energy bin of 63 keV). In addition, there were provisions to identify and remove electron precipitation events driven by field-line curvature scattering, EMIC-driven precipitation, and microbursts. Curvature scattering (Imhof et al., 1977; Sergeev et al., 1983; Büchner & Zelenyi, 1989) of plasma sheet and radiation belt electrons can be identified by its sharp energy/latitude dispersion (isotropy boundary) that results in high precipitating-to-trapped flux ratio at relativistic energies closer to the planet (see the IB precipitating pattern in Fig. 1b and statistical results in Wilkins et al. (2023)). Such data, in addition to the isotropic precipitation with $j_{prec}/j_{trap} \sim 1$ of < 300 keV electrons poleward from the isotropy boundary (Artemyev et al., 2022), are removed from our statistics. Next, electromagnetic ion cyclotron (EMIC) waves, which are caused by nightside ion injections (Jun et al., 2019; Kim et al., 2021) and efficiently scatter and precipitate relativistic electrons (e.g., Blum, Halford, et al., 2015; Blum, Li, & Denton, 2015; Yahnin et al., 2016, 2017; Capannolo et al., 2019, 2023), are excluded. These EMIC-driven observations are identified by precipitating-to-trapped ratios that reach their peak at $\geq$ 500 keV energy (see examples in X. An et al., 2022; Grach et al., 2022; Capannolo et al., 2023; Angelopoulos et al., 2023). Additionally, whistler-mode hiss waves provide a wide energy range of scattering, from weak scattering further from the plasmasphere to precipitation of relativistic electrons within the plasmasphere (see discussion of ELFIN observations of such precipitation in Mourenas et al., 2021; Angelopoulos et al., 2023; X.-C. Shen et al., 2023); these hiss precipitation events are also eliminated. Figure 1e shows this particular pattern, which is recognizable by a low j_{prec}/j_{trap} ratio peaking at ≥ 500 keV energy at low L-shells. Finally, we exclude all precipitation patterns showing microburst-like flux variation within one spin (such events are characterized by precipitating-to-trapped flux ratio exceeding one for relativistic electron energies, see X.-J. Zhang et al., 2022, for further examples).

All these effects are programmatically eliminated from statistics leaving us with only one type of precipitating energy distribution: a precipitating-to-trapped ratio monotonically decreasing with energy, observed primarily within L-shells $\in [4, 8]$, corresponding to the outer radiation belt outside the plasmasphere (e.g., Mourenas et al., 2021). This type of precipitation can only be caused by whistler-mode waves (see more details and examples in Tsai et al., 2022; X.-J. Zhang et al., 2022, 2023), and is demonstrated in Figure 1(b,e).

We combine all ELFIN observations from the nightside MLT sector (27950 spins across 4458 radiation belt crossings) and plot the averaged precipitating-to-trapped flux spectra for three geomagnetic activity levels and two L-shell domains ($4.5-5.5$ and $5.5-7.5$) for $AE \in [100, 300]$ nT in Fig. 2d. Fig. 2(a-c) show that the precipitating-to-trapped electron flux ratio j_{prec}/j_{trap} above 100 keV increases significantly as AE increases. The precipitating-to-trapped flux ratio reaches $j_{prec}/j_{trap} \sim 0.1$ up to $200-400$ keV when $AE > 300$ nT. This result is consistent with past observations of stronger energetic electron injections from the plasma sheet during periods of higher AE (Tao et al., 2011; Runov et al., 2015; Gabrielse et al., 2014), leading to even more intense whistler-mode waves (Meredith et al., 2001; X. J. Zhang et al., 2018) which can efficiently precipitate $50-500$ keV electrons (Summers et al., 2004; Thorne et al., 2005; Aryan et al., 2020; Agapitov et al., 2018). The ratio j_{prec}/j_{trap} is also higher at $L = 5.5-7.5$ than at $L = 4.5-5.5$ in Fig. 2, in agreement with the higher chorus wave power at higher $L > 5.0-5.5$ in the night sector in spacecraft statistics (Agapitov et al., 2018; Meredith et al., 2020). The smooth decrease of j_{prec}/j_{trap} as electron energy increases in Fig. 2d is consistent with the expectation that at higher latitudes, wave power decreases while minimum cy-

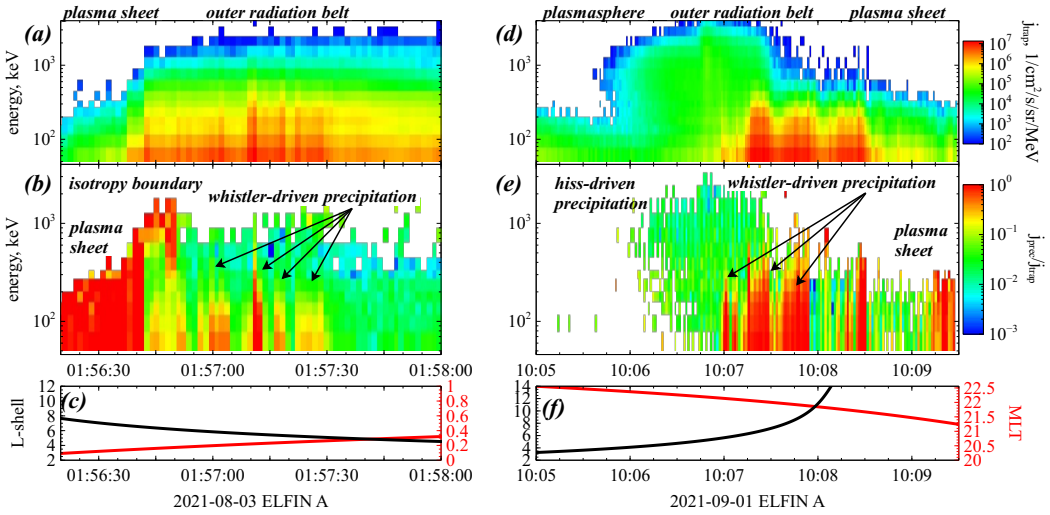

Figure 1. Two examples of ELFIN observations with strong precipitation of energetic electrons in the nightside MLT sector showing locally trapped electron fluxes (a,d), precipitating-to-trapped flux ratio (b,e), and ELFIN's MLT, L-shell coordinates from (Tsyganenko, 1989) model (c,f).

clotron resonance energy increases, therefore precipitating higher energy electrons at lower absolute flux levels (Agapitov et al., 2018; Meredith et al., 2020).

3 Simulation

Calculating the precipitating-to-trapped flux ratios is useful because it eliminates the trapped flux variability (which can vary by orders of magnitude). The slope of the ratio's energy spectra now represents only the relative effects of resonant interactions with whistler-mode waves. To then compare with ELFIN statistics, we obtain modeled precipitating-to-trapped flux ratios using two different types of simulations: (1) a configurable large-ensemble test particle simulation for electron resonant interactions, as used in previous work (Tsai et al., 2022, 2023) and (2) a quasi-linear diffusion code which has been used in previous radiation belt simulations (Ma et al., 2012, 2015). The test particle simulations include potential non-linear resonant effects and consider only purely monochromatic waves, whereas the quasi-linear diffusion code models electron scattering by an ensemble of oblique waves with higher order resonant interactions across a distribution of frequencies. Thus, by comparing results obtained by these two approahces, we can fully capture the importance of different resonant effects for electron scattering and losses.

3.1 Test particle simulation

Our test particle simulation (Tsai et al., 2022, 2023) is designed to compute the expected energy distribution of the electron precipitation flux ratio given realistic wave parameters. In order to obtain enough statistics – especially at higher energies where it is less likely for electrons to be scattered into the loss cone – we use a large number of particles for all test particle simulations in this study with $N = 5 \times 10^6$. For this to run in a reasonable amount of time, we parallelize the code and implement it in Julia 1.9.3 (Bezanson et al., 2017) using the differential equations package (Rackauckas & Nie, 2017). The Hamiltonian formulation for wave-particle resonant interactions (Albert et al., 2013; Vainchtein et al., 2018) incorporates nonlinear effects such as phase bunch-

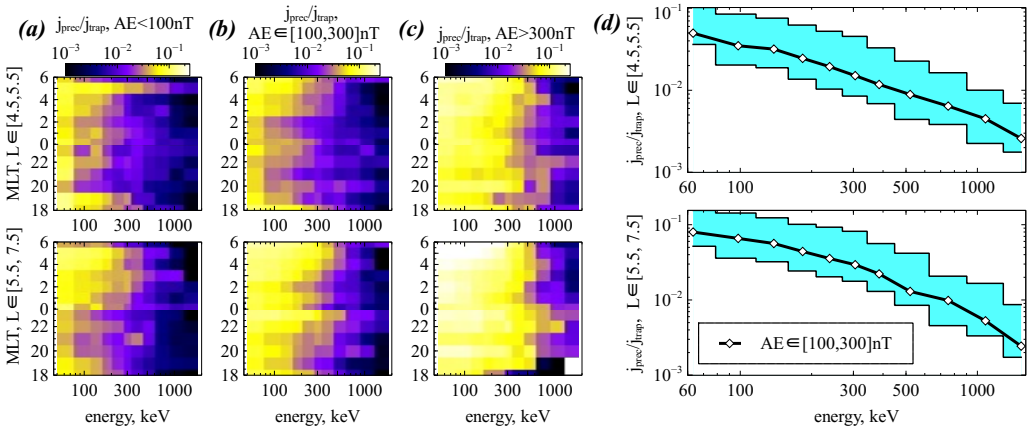

Figure 2. Plots (a-c) show the statistical distributions of precipitating-to-trapped electron spectra in (MLT, energy) space for several levels of geomagnetic activity. Plots (d) show energy profiles of precipitating-to-trapped fluxes for three geomagnetic activity levels in the nightside MLT $\in$ [18, 4]. The shaded blue range regions represent the upper (AE > 300 nT) and lower (AE < 100 nT) bounds of geomagnetic activity levels while the central black curve depicts AE $\in [100, 300]$ nT.

ing, phase trapping, and anomalous trapping (Demekhov et al., 2006; Bortnik et al., 2008; Katoh et al., 2008; Omura et al., 2007; Kitahara & Katoh, 2019; Albert et al., 2021). The simulation uses monochromatic waves, which is generally valid for describing diffusive scattering in a background dipolar magnetic field due to its strong magnetic field gradient (Albert, 2001, 2010; Shklyar, 2021). Critically, the wave field is modified by the function $B_w(\lambda, \mathrm{L}, \mathrm{MLT}, \mathrm{Kp})$ which describes the wave amplitude variation along magnetic field lines using an empirical chorus wave model built using 14 years of Cluster and Van Allen Probe statistics. The wave model is dependent on latitude, geographic location, and geomagnetic activity (see model and coefficients in Agapitov et al., 2018), which is necessary for realistic modeling of energetic electron losses. Further details of the test particle simulation implementation can be found in Tsai et al. (2022, 2023).

In this study, we have further augmented the test particle simulation to explore the latitudinal dependence of wave frequency and obliquity so that wave frequency $\omega(\lambda, \theta)$ is a function of both latitude and wave normal angle. Changing into dimensionless variables allows us to provide a mean normalized wave frequency $\omega_m(\lambda) = \omega(\lambda)/\Omega_{ce,eq}$ and mean wave normal angle $\theta(\lambda)$ both as functions of magnetic latitude λ (as described in Section 3.3). With dimensionless variables, the normalized plasma frequency is defined as $\Omega_{pe} = \omega_{pe,eq}/\Omega_{ce,eq}$.

3.2 Quasi-linear diffusion code

To instill further confidence in test particle simulation results, we calculate the quasi-linear diffusion coefficients using the Full Diffusion Code (Ni et al., 2008, 2011; Shprits & Ni, 2009; Ma et al., 2018) and model the precipitating electron flux using the Fokker-Planck diffusion code (Ma et al., 2012, 2015). This quasi-linear diffusion code physically differs from the test particle simulations primarily in the fact that it prescribes Gaussian distributions for the wave frequency (Glauert & Horne, 2005):

$$\hat{B}^2(\omega) \sim \exp\left[-\frac{(\omega - \omega_m(\lambda))^2}{\delta\omega^2}\right]$$

and the wave normal angle:

$$g(\theta) \sim \exp\left[-\frac{\left(\tan\theta - \tan\theta_m(\lambda)\right)^2}{(\tan\delta\theta)^2}\right]$$

where mean values ω_m and θ_m with bandwidths $\delta\omega$ and $\delta\theta$ represent wave frequency and normal angle, respectively. These distributions are provided relative to mean values, $\omega_m(\lambda)$ and $\theta_m(\lambda)$, which are given as functions of magnetic latitude λ and discussed in the next section (see details in Artemyev et al., 2013; Agapitov et al., 2018; Aryan et al., 2020).

We use the bounce-averaged Fokker-Planck equation to model the electron precipitation rate (Lyons et al., 1972; Glauert & Horne, 2005):

$$\frac{\partial f}{\partial t} = \frac{1}{\tau_b(\alpha_{eq})\sin 2\alpha_{eq}}\frac{\partial}{\partial \alpha_{eq}}\left(\tau_b(\alpha_{eq})\sin 2\alpha_{eq}\left(\langle D_{\alpha\alpha}\rangle\frac{\partial f}{\partial \alpha_{eq}}\right)\right) - \frac{f}{\tau_{loss}} \quad (1)$$

where α_{eq} is the equatorial pitch angle, $\tau_b \approx 1.38-0.32\left(\sin\alpha_{eq} + \sin^2\alpha_{eq}\right)$ (see Orlova & Shprits, 2011), $\langle D_{\alpha\alpha}\rangle$ is the bounce-averaged diffusion rate, and $\tau_{loss}(t)$ is the bounce loss time (and is set to be a quarter of the bounce period inside the local loss-cone and infinity outside the loss cone). We use the quasi-linear diffusion code to numerically solve Eq. (1), with diffusion rates derived from $\hat{B}^2(\omega)$ and $g(\theta)$ distributions (see Ni et al., 2008, 2011; Ma et al., 2015, 2018). Zero-gradient boundary conditions in pitch angle are set to simulate the loss cone filling of electrons due to wave scattering (Ma et al., 2022).

3.3 Frequency and Obliquity Models

In both simulations, we use the following two models to compare the effects of whistler wave frequency (normalized to the equatorial gyrofreqency) $\omega_m = \omega/\Omega_{ce,eq}$:

Model 1: normalized wave frequency held constant at $\omega_m = 0.35$, the typical frequency of whistler mode chorus waves near the equator (Agapitov et al., 2018).

Model 2: function $\omega(\lambda)$ linearly decreasing from $0.41\Omega_{ce,eq}$ at the equator until reaching a constant $0.16\Omega_{ce,eq}$ for $\lambda \geq 20°$. This model is based on statistics of off-equatorial parallel and oblique lower-band chorus waves from the Van Allen Probes (Agapitov et al., 2018).

We use the following four models to describe the mean wave normal angle (WNA) θ_m. A scaling factor $\Theta(\lambda) = \lambda/(15°+\lambda)$ is adopted to modify the WNA increase from 0 at the equator to $\Theta(45°) = 0.75$ at 45° latitude in WNA1 and WNA2.

FAW: a field-aligned wave model (with $\theta = 0°$ in test particle simulations and $\theta_m = 0°$, $\delta\theta = 30°$ or $\delta\theta = 5°$ in the quasi-linear diffusion code) that describes the most intense population of waves (Li, Santolik, et al., 2016; Agapitov et al., 2013) as they remain field-aligned off equator due to wave ducting by small-scale density structures (Hanzelka & Santolík, 2019; Y. Shen et al., 2021; Ke et al., 2021; Hosseini et al., 2021).

WNA1: a moderately oblique WNA model with $\theta_1(\lambda) = \theta_G(\lambda)\cdot\Theta(\lambda)$, where $\theta_G = \arccos(2\omega/\Omega_{ce})$ is the Gendrin angle (Gendrin, 1961). This model describes field-aligned waves that are generated at the equator, but become mildly oblique as they propagate through the inhomogeneous plasma (e.g. Breuillard et al., 2012; L. Chen et al., 2013; Ke et al., 2017).

WNA2: a very oblique WNA model with $\theta_2(\lambda) = \theta_r(\lambda)\cdot\Theta(\lambda)$, where $\theta_r = \arccos(\omega/\Omega_{ce})$ is the resonance cone angle. This describes field-aligned waves that are generated at the equator, but become very oblique as they propagate through the inhomogeneous plasma in the case of suppressed Landau damping (see discussion in Artemyev & Mourenas, 2020).

WNA3: an extremely oblique WNA model with $\theta_3(\lambda) = \theta_r(\lambda) - 2°$. This model describes very oblique waves that are generated in the equatorial source region in the presence of field-aligned electron streams suppressing Landau damping (Mourenas et al., 2015; Li, Mourenas, et al., 2016; R. Chen et al., 2019; Kong et al., 2021).

The quasi-linear simulations also require a bandwidth parameter which sets the width of the wave frequency and normal angle Gaussian distributions, defined in Section 3.2. Frequency bandwidth $\delta\omega$ is set to 0.125, and the lower and upper cutoff frequencies are set to be $\omega_m - 2\delta\omega$ and 0.5, respectively. Wave normal angle bandwidth is set to either $\delta\theta = 5°$ or $\delta\theta = 30°$ for FAW, and $\delta\theta = 10°$ for the other models; if $\theta_r(\lambda) - \theta_m(\lambda) < 20°$, we set $\delta\theta = (\theta_r(\lambda) - \theta_m(\lambda))/2$. The lower ($\theta_{LC}$) and upper ($\theta_{UC}$) cutoff wave normal angles are set as $\tan\theta_{LC} = \max(0, \tan\theta_m - 2\tan\delta\theta)$ and $\tan\theta_{UC} = \min(\tan 89.9°, \tan\theta_m + 2\tan\delta\theta)$, respectively.

Finally, the magnetic wave power distribution $B_w^2(\lambda)$ is taken from an empirical statistical model (Agapitov et al., 2018) at 23 MLT and $L = 6$ for $Kp = 3$. Note that we use $Kp = 3$ as a reasonable estimate of average geomagnetic activity level for ELFIN observations of electron precipitation driven by resonance with whistler-mode waves (see Tsai et al., 2023, for further discussion). For quiet conditions $Kp \leq 2$, the wave intensity provides insufficient levels of precipitating electron fluxes, which is generally corroborated by the extremely low levels (i.e. near background) of precipitating fluxes ELFIN observes during quiet periods. During disturbed storm times ($Kp > 4$), the precipitating and locally trapped fluxes are occasionally too large and approach saturation of ELFIN's EPDE instrument (see details in X.-J. Zhang et al., 2022). Both types of ELFIN observations (either background-level precipitation or nearly-saturated measurements) are excluded from the statistical analysis.

4 Data-model comparison

In this section, the precipitating-to-trapped electron flux ratio j_{prec}/j_{trap}, calculated through test particle simulations (TPS) or Quasi-Linear Diffusion Code (QLDC), are compared with j_{prec}/j_{trap} as measured by ELFIN. This allows us to assess the different roles potentially played by plasma density, wave obliquity, and wave frequency based on precipitating flux ratio variation with energy.

For proper comparison, the simulated j_{prec}/j_{trap} flux ratio is normalized to the observed j_{prec}/j_{trap} flux ratio at ELFIN's second energy bin ($\sim$ 97 keV), thereby removing wave amplitude variability such that the spectral slope can be compared for across various scenarios. This is valid because the $\sim$ 30 − 100 keV precipitating-to-trapped electron flux ratio correlates well with the equatorial wave amplitude (Li et al., 2013; Ni et al., 2014). In addition, spurious variations in j_{prec}/j_{trap} modeled using our test particle simulations tend to become larger below 97 keV, despite the large number of particle runs per energy bin. These oscillations are absent from results of the quasi-linear diffusion code, which correlate well with test particle simulation results above 97 keV after normalization.

4.1 Role of plasma density

Figure 3 shows a comparison between the precipitating-to-trapped electron flux ratio j_{prec}/j_{trap} measured by ELFIN at $L > 5$ and 18-4 MLT (black) with j_{prec}/j_{trap} obtained from TPS (solid red) and QLDC (dashed red) with parallel (FAW model) lower-band chorus waves (adopting $\theta = 0°$ in test particle simulations, $\delta\theta = 30°$ in the quasi-linear diffusion code), using wave frequency Model 1 of constant frequency ($\omega_m = 0.35$) chorus waves and a typical plasma frequency to gyrofrequency ratio $\Omega_{pe} = 6.5$ at $L =$ 6.5 and 23 MLT (Sheeley et al., 2001). In this plot (and remaining Figures 3-7), the gray shaded regions of ELFIN data denote the boundaries of quiet (AE $<$ 100 nT) and ac-

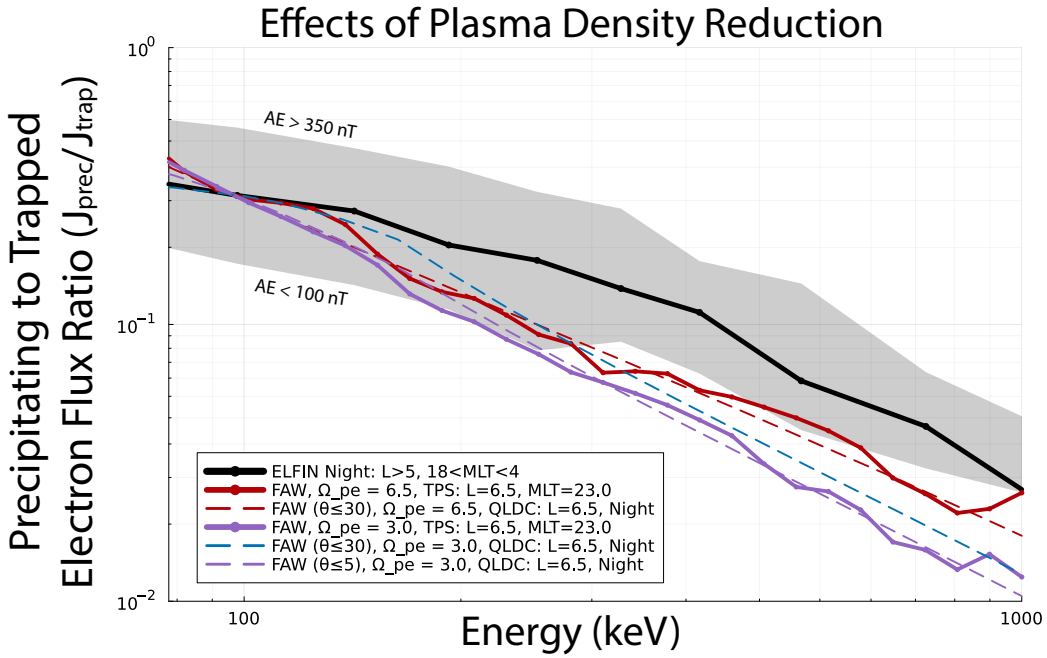

Figure 3. ELFIN-measured precipitating-to-trapped electron flux ratio at $L > 5$ on the nightside ($18 - 4$ MLT) as a function of energy (black curve). The corresponding j_{prec}/j_{trap} flux ratio obtained from test particle simulations is shown for parallel (FAW model, $\theta = 0°$) lower-band chorus waves, using frequency Model 1 ($\omega_m = constant$) and a typical $\Omega_{pe} = 6.5$ at $L = 6.5$ and 23 MLT (solid red). Results from the quasi-linear diffusion code using the same parameters is shown in dashed red. Similarly, the cases of reduced density $\Omega_{pe} = 3$ modeled with test particle simulation (solid purple), quasi-linear diffusion code using narrow-band field aligned waves ($\delta\theta = 5°$, dashed purple), and more quasi-linear field aligned waves ($\delta\theta = 30°$, dashed blue), are shown. All simulation results are normalized to observations at 97 keV.

tive (AE > 350 nT) times. The normalized ratios j_{prec}/j_{trap} obtained from TPS and QLDC are quite similar (compare solid with dashed lines of the same color), validating the reliability of the quasi-linear approach (Kennel & Engelmann, 1966; Lyons et al., 1972; Albert, 2005; Glauert & Horne, 2005; Mourenas et al., 2012; Mourenas, Artemyev, Agapitov, & Krasnoselskikh, 2014), especially in the case of field aligned waves, as demonstrated in previous studies (Tao et al., 2012; Mourenas, Artemyev, et al., 2022; Gan et al., 2022; Z. An et al., 2022). However, despite their normalization to the measured j_{prec}/j_{trap} at 97 keV, these similar ratios of j_{prec}/j_{trap} (red curves) obtained from test particle simulations and from the quasi-linear diffusion code become $\sim 1.5-2$ times smaller than the measured j_{prec}/j_{trap} at 200−1000 keV (black), corresponding to a deficiency of pitch-angle diffusion occurring at higher energies. For reference, this baseline case (red) represents the same discrepancy on the nightside as first described in Tsai et al. (2023).

A reduced plasma density should lower the latitude of first-order cyclotron resonance with chorus waves for electrons near the loss-cone (Mourenas et al., 2012). Since chorus wave power B_w^2 is higher at lower latitudes (Agapitov et al., 2018), a reduced density is therefore expected to yield higher electron pitch-angle diffusion rate $D_{\alpha\alpha} \propto B_w^2$ near the loss-cone leading to higher precipitation rates and fluxes at all energies. However, adopting a reduced plasma density ($\Omega_{pe} = 3$) in test particle simulations (purple line in Fig. 3) and normalizing the flux ratio at 97 keV leads to an even larger discrepancy across the $300-1000$ keV range with a $\sim 2-3$ times smaller j_{prec}/j_{trap} ratio than ELFIN statistics show. We therefore interpret this density effect as more important at lower energies ($\sim$ 100 keV) compared to higher energies ($>$ 300 keV) due to $B_w^2(\lambda)$ increasing, in our model and in observations, more steeply towards lower latitudes at $\lambda \lesssim 25°$ (where resonance with ~ 100 keV electrons occurs) than at $\lambda > 25°$ (where resonance with ~ 1 MeV electrons occurs) during disturbed periods at 21-3 MLT (Agapitov et al., 2018). Therefore, the wave power $B_w^2(\lambda)$ seen by electrons near the loss-cone increases only marginally at higher energies for both $\theta = 0°$ in test-particle simulations and $\theta < 5°$ or $\theta < 30°$ in QLDC simulations (solid/dashed purple and dashed blue lines). This then reduces the normalized pitch-angle diffusion rate $D_{\alpha\alpha}$ near the loss-cone and the normalized j_{prec}/j_{trap} flux ratio, which varies roughly like $\approx \sqrt{D_{\alpha\alpha}}$ (Kennel & Petschek, 1966; Li et al., 2013; Mourenas, Zhang, et al., 2022; Mourenas et al., 2023).

Adopting a more realistic spread of WNAs for quasi-field aligned waves ($\delta\theta = 30°$, blue dashed line) in the quasi-linear diffusion code leads to the effects of additional, higher-order cyclotron resonances to become more significant (Artemyev et al., 2016), which is clearly shown as the difference between the blue and purple dashed lines in Figure 3. Due to moderate obliqueness, this effect is most prominent in the lower energies – resonating with waves around the equator – extending now to about 180 keV. However, it is not enough to reproduce ELFIN observations up to 1 MeV, because the relative scattering efficiency decreases with the purple curve at higher energies, causing the blue curve to underestimate ELFIN statistics beyond $>$ 250 keV. Despite the fact that, in observations, the plasma frequency to gyrofrequency ratio Ω_{pe} does decrease at 18-4 MLT during disturbed periods (O'Brien & Moldwin, 2003), often down to $\Omega_{pe} \approx 3-4$ at $L \sim 6$ when $AE > 150$ nT (Agapitov et al., 2019), results in Figure 3 show that plasma density reduction alone cannot account for a relative increase of electron scattering at higher energies.

4.2 Role of wave frequency

As noted earlier, statistical observations of lower-band chorus waves show that their normalized frequency is not constant as a function of latitude (as assumed in frequency Model 1), but rather, decreasing due to preferential Landau damping affecting higher frequencies at higher latitudes (Agapitov et al., 2018; Bunch et al., 2013; L. Chen et al., 2013), as reflected by frequency Model 2. Figure 4a shows that the j_{prec}/j_{trap} ratios obtained for wave normal angle model FAW from test particle simulations (solid curves)

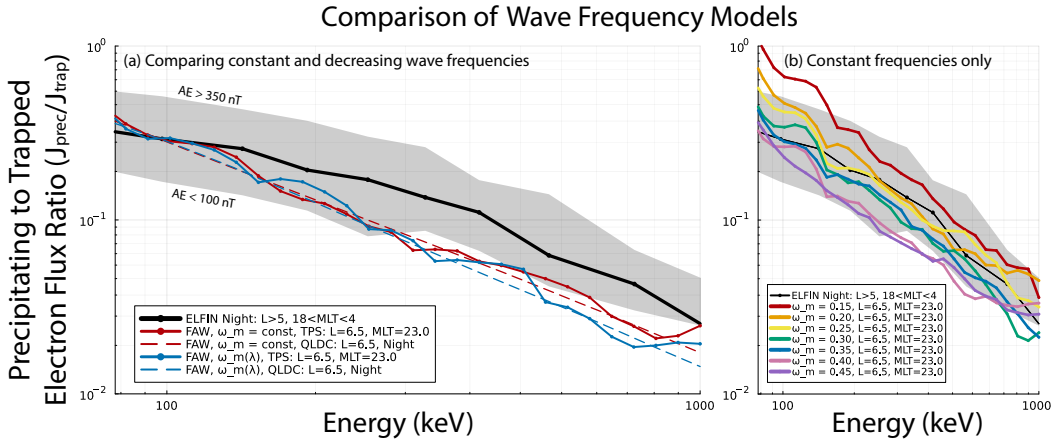

Figure 4. To compare the effects of two frequency models, precipitating-to-trapped electron flux ratio j_{prec}/j_{trap} plotted for ELFIN statistics on the nightside (black) is shown in comparison with j_{prec}/j_{trap} ratios obtained from test particle simulations (TPS, solid lines) and quasi-linear diffusion code (QLDC, dashed lines). In (a), Frequency Model 2 (frequency decreasing toward higher latitudes, blue) produces slightly higher precipitation rates at 100 keV relative to 1 MeV as compared to a constant $\omega_m = 0.35$ (red). Plot (b) shows results from a variety of normalized wave frequency values that do not vary as a function of magnetic latitude, demonstrating that absolute frequency has little effect on the slope of the precipitation energy spectra.

and from the quasi-linear diffusion code (dashed curves) are both slightly decreased at $E = 200 - 1000$ keV when wave frequency Model 2 is used (blue curves), rather than when using Model 1. This is because a reduction of wave frequency alone, when adopting a fixed plasma density $\Omega_{pe} = 6.5$ at $L = 6.5$, has essentially the same effect as decreasing plasma density in Section 4.1 – albeit weaker in magnitude – by allowing first-order cyclotron resonance for electrons near the loss-cone to occur at lower latitudes (Mourenas et al., 2012). In turn, this preferentially increases precipitation rates at low energies $E \lesssim$ 100 keV, the typical resonance energies at low-latitude plasma conditions.

Figure 4b shows that decreasing the wave frequency by a fixed amount significantly increases electron precipitation rates by lowering the latitude of resonance with chorus waves. But at the same time, it leads to only a slight increase of the slope of the energy spectrum once normalized to ELFIN statistics, because the amplitude of resonant waves is slightly more increased for 100 keV electrons than for 1 MeV electrons. For a large plasma density, $\Omega_{pe} = 6.5$, this effect on the normalized j_{prec}/j_{trap} remains weak, and both wave frequency Model 1 and 2 end up giving very similar results. Therefore, the effects of frequency variation with latitude alone cannot account for the spectral shape of the precipitation ratio in ELFIN's nightside observations.

4.3 Role of wave obliquity

Figure 5a compares ELFIN-observed precipitating-to-trapped flux ratio on the nightside (black) with that of simulations in order to explore the effects of a variety of wave-normal angle distributions paired with constant wave frequency (Model 1) and baseline plasma density (Sheeley et al., 2001). Results from test particle simulations (solid curves) and from the quasi-linear diffusion code (dashed curves) are displayed for four different models of wave normal angle: FAW (red), WNA1 (green), WNA2 (blue), and WNA3 (purple), corresponding to a progressively larger amount of wave power in oblique waves closer to the resonance cone angle (see Section 3.3). Despite the large number of particles ($N =$

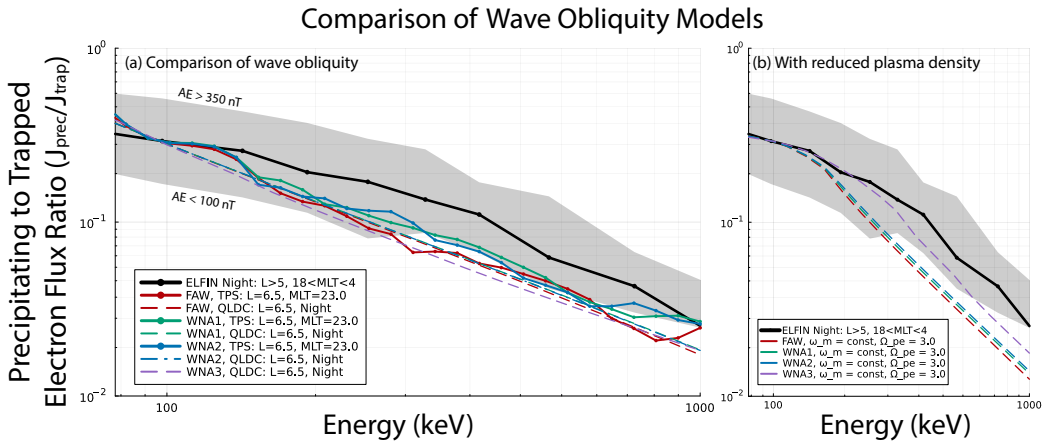

Figure 5. ELFIN-observed j_{prec}/j_{trap} flux ratio at $L > 5$ on the nightside (18 − 4 MLT) as a function of electron energy (black). The corresponding ratios j_{prec}/j_{trap} obtained from test particle simulations (TPS, solid curves) and from the quasi-linear diffusion code (QLDC, dashed curves) are displayed for lower-band chorus waves in (a), using frequency Model 1 of constant frequency, and parameterized by four wave normal angle models: FAW (red), WNA1 (green), WNA2 (blue), and WNA3 (purple), with a normalization to observations at 97 keV, adopting a typical $\Omega_{pe} = 6.5$ at $L = 6.5$ and 23 MLT. (b) shows QLDC results for the same four wave normal angle models but for a reduced plasma density of $\Omega_{pe} = 3.0$.

5×10^6), unnatural oscillations in the test particle simulations make it difficult to quantify the exact contribution differences among the FAW, WNA1, and WNA2 models. Especially because the test particle simulation only includes first-order oblique wave interactions, it is reasonable to conclude that including wave obliquity in the TPS does not significantly alter precipitation efficiency. However, results from the quasi-linear diffusion code generally agree with test particle simulation results, indicating the reliability of the quasi-linear approach (described, e.g., by Kennel & Engelmann, 1966; Lyons et al., 1972; Albert, 2005; Glauert & Horne, 2005; Mourenas et al., 2012; Mourenas, Artemyev, Agapitov, & Krasnoselskikh, 2014). Our quasi-linear simulations show that wave obliquity is ineffective at increasing high energy electron precipitation compared to low energy electron precipitation (in the case of $\Omega_{pe} = 6.5$). Note that WNA1 and WNA2 models correspond to wave-normal angle distributions that extend up to three-quarters of the Gendrin angle and resonance cone angle, respectively, at $\lambda > 45°$, while the WNA3 model corresponds to highly oblique waves, at about 2° from the resonance cone angle. Yet the results are nearly identical (dashed blue, dashed green, and dashed purple curves).

Oblique chorus waves can resonate with electrons via high-order cyclotron resonances ($n \geq 1$ or $n \leq -2$, e.g., Shklyar & Matsumoto, 2009; Mourenas et al., 2012; Artemyev et al., 2013, 2016; Albert, 2017), which can significantly increase diffusion rates at high energy (Lorentzen et al., 2001; Gan et al., 2023). However, diffusion rates near the loss cone due to higher-order cyclotron resonances rapidly decrease in magnitude as $|n|$ increases, especially from $|n| = 1$ to $|n| = 2$ (Shprits & Ni, 2009), although this reduction is weaker for highly oblique waves (Artemyev et al., 2016). To increase the ratio of 1 MeV to 100 keV pitch-angle diffusion rates near the loss cone, therefore, the waves must be sufficiently oblique and/or plasma density and wave frequency should be sufficiently low to enable only first-order resonance at $\sim$ 100 keV, but higher-order resonances at 1 MeV (Artemyev et al., 2016; Mourenas & Ripoll, 2012; Shprits & Ni, 2009; Gan et al., 2023). Figure 5b indeed shows that when plasma density is reduced to $\Omega_{pe} = 3$ (or equiv-

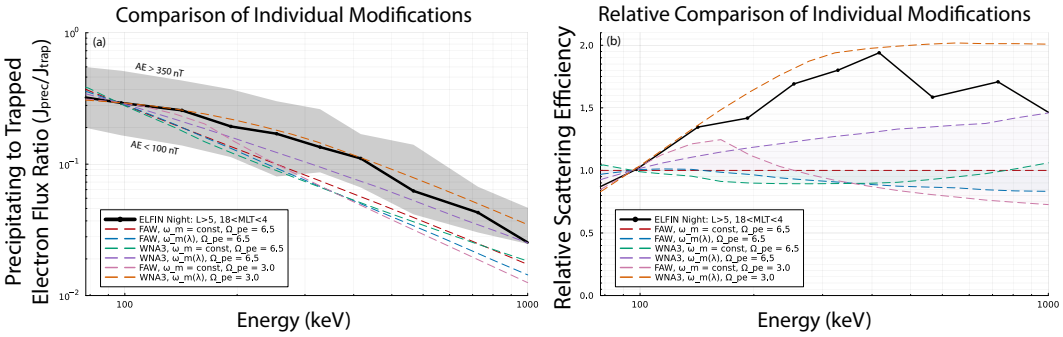

Figure 6. ELFIN-observed nightside ($18 - 4$ MLT) j_{prec}/j_{trap} electron flux ratio shown as a function of energy (black). (a) shows j_{prec}/j_{trap} flux ratios obtained from quasi-linear diffusion code (QLDC) for parallel (FAW) lower-band chorus waves (red), very oblique waves using wave normal angle model WNA3 (green), waves with a realistic wave frequency distribution (blue), WNA3 with a realistic wave frequency distribution (purple), FAW with reduced density (pink), and everything combined (orange). (b) shows the same flux ratios all normalized to the base case with no modifications (red) demonstrating which energy range each modification is most effective at on a linear scale. This shows that each effect examined alone cannot reproduce results from ELFIN individually.

alently, when wave frequency decreases with latitude, see Section 4.4), electron precipitation is greatly increased at 1 MeV relative to 100 keV as wave obliquity increases, especially in the case of highly oblique waves (WNA3). These results therefore suggest that wave obliquity, alone, has a near-negligible effect on the high-energy to low-energy electron loss ratio; however, when combined with a density reduction, it can significantly enhance energetic electron losses.

4.4 Combined results

Figure 6a shows comparisons between the precipitating-to-trapped electron flux ratio j_{prec}/j_{trap} measured by ELFIN at $L > 5$ on the nightside (black), overlaid with j_{prec}/j_{trap} obtained from the quasi-linear diffusion code for the three modifications in question – reduced plasma density $\Omega_{pe} = 3$, Frequency Model 2, and WNA3 – alone or in combination. As surmised in previous sections, each individual modification fails to agree with the observed spectrum. With wave frequency Model 2 (blue) and WNA3 (green) underestimating across entire energy range (i.e., increasing precipitation at 100 keV) and reduced density (pink) providing a relative efficiency bump of j_{prec}/j_{trap} only at $E <$ 200 keV. Interestingly, however, ELFIN's statistical observations are only slightly underestimated when combining WNA3 and Frequency Model 2 (purple), and best matched when all three modifications are combined (orange). Figure 6b shows the relative difference produced by each modification compared to the baseline red curve. We see that these effects synergistically enhance j_{prec}/j_{trap} flux ratios at higher energies. For example, Model 2 (blue) becomes relatively less effective at higher energy, while WNA3 (green) immediately loses effectiveness, but catches back up closer to 1 MeV. However, when combined (purple), the relative precipitation is drastically enhanced in the entire $200-1000$ keV range, leading to far better agreement with observations. Further combining WNA3 and Frequency Model 2 with a reduced plasma density (orange) significantly enhances precipitation past levels observed by ELFIN (black). This is likely due to two phenomena: first, the combined effects of a reduced plasma density and a decreasing wave frequency decrease the latitude at which cyclotron resonance with quasi-parallel waves oc-

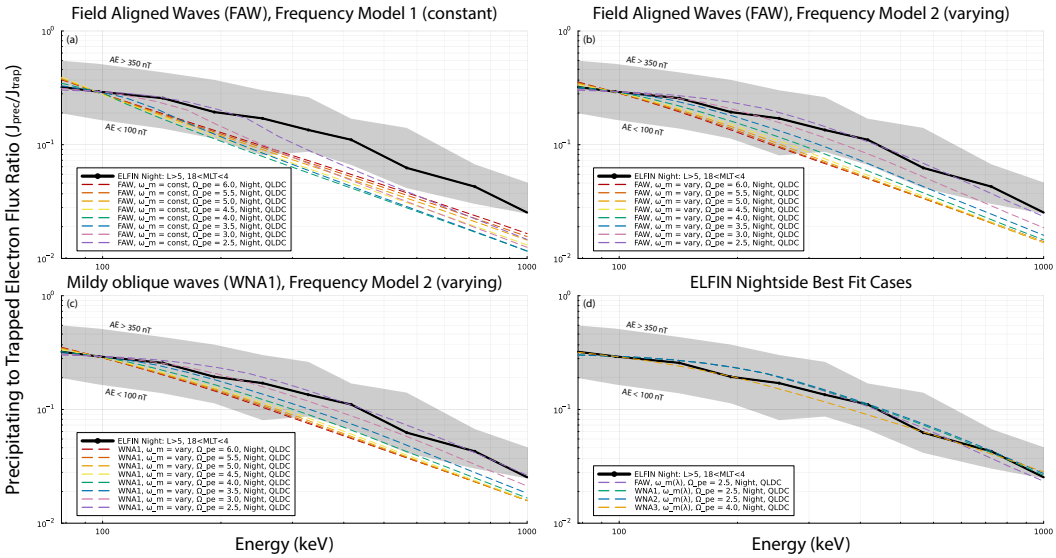

Figure 7. The comparison between observed electron precipitation ratios and simulation results using different wave frequency models, Ω_{pe} ratios, and wave normal angle models. In each plot, the black line denotes statistical averages of j_{prec}/j_{trap} flux ratios for nightside ELFIN observations with $L > 5$. Plots (a-c) show QLDC results with various modifications parameterized by Ω_{pe}: (a) shows field aligned waves with Frequency Model 1; (b) shows field aligned waves with Frequency Model 2; and (c) shows WNA1 combined with Frequency Model 2. (d) shows that all three effects – $\omega_{pe} \in [2.5, 4]$, combined with Frequency Model 2 and some level of wave obliquity – are necessary for recreating ELFIN nightside statistics.

curs far more significantly than each effect alone (Mourenas et al., 2012), leading to a larger increase of resonant wave power for higher energy electrons that best match ELFIN's observed precipitation spectra; second, the supplementary higher-order cyclotron resonances contributing at $\sim$ 1 MeV, but not at $\sim$ 150 keV, are of lower order ($|n| = 2$) than for higher density or frequency, allowing for a more dramatic increase of the 1 MeV to 150 keV pitch-angle diffusion rate ratio (Artemyev et al., 2016; Mourenas & Ripoll, 2012; Shprits & Ni, 2009; Gan et al., 2023).

Figure 7 summarizes the findings from each wave parameter combination throughout a range of reduced equatorial plasma densities for a better understanding of the interplay between the three effects considered. Figure 7a shows that only below a certain threshold of $\Omega_{pe} \lesssim 4$ does the interaction of higher-order resonances start to increase precipitation at higher energies. Using the total electron density with $\Omega_{pe} = 2.5$, this effect becomes very pronounced above 100 keV and up to 300 keV, whereas above that energy this effect alone is still incapable of matching observations, as discussed in Section 4.1. The effect of plasma density combined with wave frequency becomes significantly more pronounced throughout the whole energy range when $\Omega_{pe} \lesssim 4$, as shown in Figure 7b, and matches very well with ELFIN's nightside observations when a more extreme $\Omega_{pe} = 2.5$ is used. Adding mild wave obliquity (Figure 7c) results in the best match with ELFIN statistics, demonstrating that all three effects combined are necessary.

Figure 7d shows the best fit scenarios for forward-modeling ELFIN-observed precipitating-to-trapped flux ratios, which all require the varying frequency model in addition to reduced plasma density to various degrees. Here, we show that it is possible to obtain decent agreement without the need for wave obliquity by significantly reducing Ω_{pe} to 2.5

(purple). By adding moderately oblique waves (green and blue), more ~ 1 MeV electrons are precipitated, doing a marginally better job of matching observations. Using extremely oblique waves (WNA3) – which describes a population of very oblique waves generated around the equator when the Landau damping is largely reduced by field-aligned electron streams (Mourenas et al., 2015; Li, Mourenas, et al., 2016) – requires increasing plasma density $\Omega_{pe} = 4$ in order to avoid significant overestimation. Therefore, ELFIN observations of nightside electron precipitation spectra (from $50-1000$ keV) can be described either under the assumption of a significant plasma density reduction or a more moderate plasma density reduction coupled with a strongly oblique wave population. This required plasma density ($\omega_{pe} \in [2.5, 4]$) is fully consistent with the average measured ω_{pe} levels at 18-4 MLT and $L = 5-6.5$ in Van Allen Probes statistics during disturbed periods with $AE \in [150, 600]$ nT (Agapitov et al., 2019). These conditions indicate the importance of plasma injections and/or enhanced convection periods and how they cause enhanced nightside electron losses. Such Earthward plasma transport (convection and injections), especially during increased geomagnetic activity, justifies our choice of the cold plasma density reduction (Agapitov et al., 2019). These injections are also associated with electron field-aligned streams caused by the electrostatic turbulence around injection regions or the ionosphere outflow of secondary electrons in response to the enhanced precipitation of plasma sheet electron fluxes (see Khazanov et al., 2014, 2018; Artemyev & Mourenas, 2020; Artemyev et al., 2020, and references therein).

5 Discussion and Conclusions

Today's radiation belt simulations primarily rely on EMIC-driven electron precipitation to explain relativistic electron losses (see, e.g., Ma et al., 2015; Drozdov et al., 2017, and references therein), in addition to dropouts related to magnetopause shadowing loss (e.g., see Shprits et al., 2006; Turner et al., 2014; Boynton et al., 2016, 2017; Olifer et al., 2018; Xiang et al., 2018). Analysis presented here shows that the inclusion of realistic whistler-mode wave properties can meaningfully enhance relativistic electron scattering rates, thereby reducing the relative importance of EMIC waves on the nightside, at least for electrons below 1 MeV. While it has been known for a long time that whistler-mode waves can accelerate electrons to relativistic energies (Thorne et al., 2013; Li et al., 2014; Mourenas, Artemyev, Agapitov, Krasnoselskikh, & Li, 2014; Omura et al., 2015; Hsieh & Omura, 2017; Allison & Shprits, 2020), contribution of this wave mode to relativistic electron losses may be underestimated in modern-day simulations due to the lack of observations that can reliably quantify it. This has recently changed with the availability of ELFIN's unique precipitation observations, which now allow us to quantify how well modeling – based on statistical averages of wave proprties and plasma density – reflects the observed precipitation energy spectra of energetic electrons.

We previously showed that using only field-aligned, monochromatic whistler-mode waves with realistic wave amplitudes as a function of magnetic latitude was sufficient to approximate relativistic electron losses at the dawn, noon, and dusk sectors (Tsai et al., 2023). However, the modeled precipitating-to-trapped flux ratio significantly underestimated ELFIN-obtained statistics of precipitation energy spectra in the nightside MLT sector. Pertinent to ELFIN statistics, we specifically excluded all data exhibiting signatures of field-line curvature scattering, EMIC waves, and any signatures of noise or poor statistics. The resulting ELFIN statistics are 3 years of unambiguous whistler-mode wave-driven energetic electron precipitating-to-trapped flux ratios across a range of MLT, L-shells, and geomagnetic activity. At first, we used test particle simulations to examine various wave and plasma characteristics that may potentially cause this discrepancy. However, test particle simulations showed that, while some effects led to better agreement, the discrepancy was still large. However, by additionally utilizing a state-of-the-art quasi-linear diffusion code, we were able to quantify each key wave parameter – alone and in combination – relative to ELFIN observations, thereby determining the importance of

including empirically-obtained equatorial plasma frequency, wave-normal angle distributions, and wave frequency distributions. We found that, in addition to the prerequisite, empirically-provided $B_w(\lambda)$ (Tsai et al., 2023), inclusion of all three modifications – realistic Ω_{pe}, $\omega_m(\lambda)$, and $\theta(\lambda)$ – were sufficient to recover the more intense nightside energetic precipitation observed by ELFIN. A reduced plasma density, indicative of geomagnetically active times, results in relative enhancement of precipitation in the subrelativistic regime (< 300 keV), while wave obliquity significantly enhances relativistic electron scattering > 500 keV. It seems that a decreasing wave frequency as a function of latitude helps balance the two out, leading to a smooth recovery of the $200-600$ keV range, without severely overestimating either ends of the precipitation flux ratio spectrum.

The equatorial confinement of whistler-mode waves is attributed to the increase of wave obliquity – or more precisely, the increase of statistical averages of wave normal angles – as expected from wave propagation away from their equatorial source (L. Chen et al., 2013; Breuillard et al., 2012; Agapitov et al., 2013) due to the associated severe damping by Landau resonance with suprathermal electrons (e.g., Bell et al., 2002; Bortnik et al., 2007). This effect is substantially less important on the dayside as compared to the nightside, as evidenced by the significantly larger amplitudes of waves at higher latitudes on the dayside (Meredith et al., 2012). Reduced Landau damping is caused by a milder ambient dayside magnetic field gradient (due to magnetospheric compression) and a lower density of suprathermal electrons (Li, Thorne, Bortnik, et al., 2010; Walsh et al., 2020). As a result, waves on the dayside propagate in higher densities, are less oblique, and have a less pronounced decrease in wave frequencies, in direct opposition to what is observed on the nightside. This explains why an empirical model of $B_w(\lambda)$ and field aligned waves is sufficient for recovering dayside energetic electron precipitation (Tsai et al., 2023), while further indicating the importance of including realistic wave and background plasma characteristics for such precipitation modeling on the nightside.

To conclude, these results highlight the importance of combining whistler-mode wave characteristics and background plasma for accurately modeling relativistic electron losses from the outer radiation belt. Specifically, we note that:

- The latitudinal distribution of wave amplitude alone cannot account for the intense nightside precipitation of $\sim 0.1-1$ MeV electrons scattered at mid-to-high latitudes relative to precipitation of ~ 100 keV electrons scattered near the equator.
- Very oblique waves are important for scattering more energetic electrons – becoming more effective in the $\sim$ 1 MeV range – but only in the presence of reduced plasma density or decreasing wave frequency.
- The decrease of wave frequency with latitude, caused by high-frequency wave damping, is not very important on its own. However, together with a reduced plasma density (with or without oblique waves), it can lead to more precipitation of high energy electrons relative to ~ 100 keV electrons.
- Equatorial plasma density decrease during geomagnetically active conditions (characterized by enhanced whistler-mode wave intensity) improves the relative efficiency of resonant electron scattering toward the loss-cone at 100 keV compared to 1 MeV, but alone, it is in poor agreement with ELFIN statistics. However, when combined with increasing WNA and decreasing wave frequency as a function of latitude, this plasma density reduction becomes a catalyst, significantly boosting electron precipitation rates across the energy range up to 1 MeV.

So, in order to best explain the increased precipitation observed by ELFIN on the nightside, modeled whistler-mode waves must have a realistic latitudinally-dependent wave frequency model (Model 2) coupled with a reduced plasma density ($\Omega_{pe} \in [2.5, 4]$) and an associated range of wave obliquity from quasi-field aligned ($\theta < 30^\circ$) to extremely

oblique (WNA3) waves. Any further investigation of these effects likely requires either detailed and comprehensive simulations using modern ray-tracing techniques (e.g., L. Chen et al., 2021, 2022; Hosseini et al., 2021; Hanzelka & Santolík, 2022; Kang et al., 2022; Kang & Bortnik, 2022) or a new generation of satellite missions equipped to make simultaneous measurements of whistler-mode waves and precipitating/trapped electron populations.

Acknowledgments

We are grateful to NASA's CubeSat Launch Initiative and Launch Services Program for ELFIN's successful launch in the desired orbits. We acknowledge early support of ELFIN project by the AFOSR, under its University Nanosat Program, UNP-8 project, contract FA9453-12-D-0285, and by the California Space Grant program. Importantly, we acknowledge the critical contributions by numerous UCLA students who made the ELFIN mission a success. A.V.A and X.-J.Z. acknowledge support from the NASA grants 80NSSC23K0089, 80NSSC22K0522, 80NSSC23K0108, 80NSSC19K0844, 80NSSC23K0100 and NSF grant 2329897. V. A. acknowledge support from NSF grants AGS-1242918, AGS-2019950, and AGS-2329897. Q.M. acknowledges the NASA grant 80NSSC20K0196 and NSF grant AGS-2225445. The work O.V.A. was supported by NASA grants 80NNSC19K0848, 80NSSC20K0697, 80NSSC22K0433, 80NSSC22K0522, NASA's Living with a Star (LWS) program (contract 80NSSC20K0218), and by NSF grant number 1914670.

Open Research

ELFIN data is available at `https://data.elfin.ucla.edu/` and online summary plots at `https://plots.elfin.ucla.edu/summary.php`.
Data access and processing was done using SPEDAS V4.1, see Angelopoulos et al. (2019).
Test-particle simulation code is found at `https://github.com/ethantsai/nlwhistlers` (Tsai, 2023).

References

Agapitov, O. V., Artemyev, A., Krasnoselskikh, V., Khotyaintsev, Y. V., Mourenas, D., Breuillard, H., ... Rolland, G. (2013, June). Statistics of whistler mode waves in the outer radiation belt: Cluster STAFF-SA measurements. *J. Geophys. Res.*, *118*, 3407-3420. doi: 10.1002/jgra.50312

Agapitov, O. V., Krasnoselskikh, V., Mozer, F. S., Artemyev, A. V., & Volokitin, A. S. (2015, May). Generation of nonlinear electric field bursts in the outer radiation belt through the parametric decay of whistler waves. *Geophys. Res. Lett.*, *42*, 3715-3722. doi: 10.1002/2015GL064145

Agapitov, O. V., Mourenas, D., Artemyev, A., Hospodarsky, G., & Bonnell, J. W. (2019, June). Time Scales for Electron Quasi-linear Diffusion by Lower-Band Chorus Waves: The Effects of ω_{pe}/Ω_{ce} Dependence on Geomagnetic Activity. *Geophys. Res. Lett.*, *46*(12), 6178-6187. doi: 10.1029/2019GL083446

Agapitov, O. V., Mourenas, D., Artemyev, A. V., & Mozer, F. S. (2016). Exclusion principle for very oblique and parallel lower band chorus waves. *Geophys. Res. Lett.*, *43*(21), 11,112–11,120. Retrieved from `http://dx.doi.org/10.1002/2016GL071250` doi: 10.1002/2016GL071250

Agapitov, O. V., Mourenas, D., Artemyev, A. V., Mozer, F. S., Hospodarsky, G., Bonnell, J., & Krasnoselskikh, V. (2018, January). Synthetic Empirical Chorus Wave Model From Combined Van Allen Probes and Cluster Statistics. *Journal of Geophysical Research (Space Physics)*, *123*(1), 297-314. doi: 10.1002/2017JA024843

Albert, J. M. (2001, May). Comparison of pitch angle diffusion by turbulent and monochromatic whistler waves. *J. Geophys. Res.*, *106*, 8477-8482. doi: 10

.1029/2000JA000304

Albert, J. M. (2005, March). Evaluation of quasi-linear diffusion coefficients for whistler mode waves in a plasma with arbitrary density ratio. *J. Geophys. Res.*, *110*, 3218. doi: 10.1029/2004JA010844

Albert, J. M. (2010, March). Diffusion by one wave and by many waves. *J. Geophys. Res.*, *115*, 0. doi: 10.1029/2009JA014732

Albert, J. M. (2017, May). Quasi-linear diffusion coefficients for highly oblique whistler mode waves. *J. Geophys. Res.*, *122*, 5339-5354. doi: 10.1002/2017JA024124

Albert, J. M., Artemyev, A. V., Li, W., Gan, L., & Ma, Q. (2021). Models of resonant wave-particle interactions. *Journal of Geophysical Research: Space Physics*, *126*(6), e2021JA029216. doi: 10.1029/2021JA029216

Albert, J. M., Tao, X., & Bortnik, J. (2013). Aspects of Nonlinear Wave-Particle Interactions. In D. Summers, I. U. Mann, D. N. Baker, & M. Schulz (Eds.), *Dynamics of the earth's radiation belts and inner magnetosphere.* doi: 10.1029/2012GM001324

Allison, H. J., & Shprits, Y. Y. (2020, September). Local heating of radiation belt electrons to ultra-relativistic energies. *Nature Communications*, *11*, 4533. doi: 10.1038/s41467-020-18053-z

Allison, H. J., Shprits, Y. Y., Zhelavskaya, I. S., Wang, D., & Smirnov, A. G. (2021, January). Gyroresonant wave-particle interactions with chorus waves during extreme depletions of plasma density in the Van Allen radiation belts. *Science Advances*, *7*(5), eabc0380. doi: 10.1126/sciadv.abc0380

An, X., Artemyev, A., Angelopoulos, V., Zhang, X., Mourenas, D., & Bortnik, J. (2022, September). Nonresonant Scattering of Relativistic Electrons by Electromagnetic Ion Cyclotron Waves in Earth's Radiation Belts. *Phys Rev. Lett.*, *129*(13), 135101. doi: 10.1103/PhysRevLett.129.135101

An, Z., Wu, Y., & Tao, X. (2022). Electron dynamics in a chorus wave field generated from particle-in-cell simulations. *Geophys. Res. Lett.*, *49*(3), e2022GL097778. doi: 10.1029/2022GL097778

Angelopoulos, V., Cruce, P., Drozdov, A., Grimes, E. W., Hatzigeorgiu, N., King, D. A., ... Schroeder, P. (2019, January). The Space Physics Environment Data Analysis System (SPEDAS). *Space Sci. Rev.*, *215*, 9. doi: 10.1007/s11214-018-0576-4

Angelopoulos, V., Tsai, E., Bingley, L., Shaffer, C., Turner, D. L., Runov, A., ... Zhang, G. Y. (2020, July). The ELFIN Mission. *Space Sci. Rev.*, *216*(5), 103. doi: 10.1007/s11214-020-00721-7

Angelopoulos, V., Zhang, X. J., Artemyev, A. V., Mourenas, D., Tsai, E., Wilkins, C., ... Zarifian, A. (2023, August). Energetic Electron Precipitation Driven by Electromagnetic Ion Cyclotron Waves from ELFIN's Low Altitude Perspective. *Space Sci. Rev.*, *219*(5), 37. doi: 10.1007/s11214-023-00984-w

Artemyev, A. V., Agapitov, O., Mourenas, D., Krasnoselskikh, V., Shastun, V., & Mozer, F. (2016, April). Oblique Whistler-Mode Waves in the Earth's Inner Magnetosphere: Energy Distribution, Origins, and Role in Radiation Belt Dynamics. *Space Sci. Rev.*, *200*(1-4), 261-355. doi: 10.1007/s11214-016-0252-5

Artemyev, A. V., Angelopoulos, V., Zhang, X. J., Runov, A., Petrukovich, A., Nakamura, R., ... Wilkins, C. (2022, October). Thinning of the Magnetotail Current Sheet Inferred From Low-Altitude Observations of Energetic Electrons. *Journal of Geophysical Research (Space Physics)*, *127*(10), e2022JA030705. doi: 10.1029/2022JA030705

Artemyev, A. V., & Mourenas, D. (2020, March). On Whistler Mode Wave Relation to Electron Field-Aligned Plateau Populations. *Journal of Geophysical Research (Space Physics)*, *125*(3), e27735. doi: 10.1029/2019JA027735

Artemyev, A. V., Mourenas, D., Agapitov, O. V., & Krasnoselskikh, V. V. (2013, April). Parametric validations of analytical lifetime estimates for radiation belt

electron diffusion by whistler waves. *Annales Geophysicae*, *31*, 599-624. doi: 10.5194/angeo-31-599-2013

Artemyev, A. V., Zhang, X. J., Angelopoulos, V., Mourenas, D., Vainchtein, D., Shen, Y., ... Runov, A. (2020, September). Ionosphere Feedback to Electron Scattering by Equatorial Whistler Mode Waves. *Journal of Geophysical Research (Space Physics)*, *125*(9), e28373. doi: 10.1029/2020JA028373

Aryan, H., Agapitov, O. V., Artemyev, A., Mourenas, D., Balikhin, M. A., Boynton, R., & Bortnik, J. (2020, August). Outer Radiation Belt Electron Lifetime Model Based on Combined Van Allen Probes and Cluster VLF Measurements. *Journal of Geophysical Research (Space Physics)*, *125*(8), e28018. doi: 10.1029/2020JA028018

Bell, T. F., Inan, U. S., Bortnik, J., & Scudder, J. D. (2002, August). The Landau damping of magnetospherically reflected whistlers within the plasmasphere. *Geophys. Res. Lett.*, *29*, 1733. doi: 10.1029/2002GL014752

Bezanson, J., Edelman, A., Karpinski, S., & Shah, V. B. (2017). Julia: A fresh approach to numerical computing. *SIAM review*, *59*(1), 65–98. Retrieved from `https://doi.org/10.1137/141000671`

Blake, J. B., & O'Brien, T. P. (2016, April). Observations of small-scale latitudinal structure in energetic electron precipitation. *Journal of Geophysical Research (Space Physics)*, *121*(4), 3031-3035. doi: 10.1002/2015JA021815

Blum, L. W., Halford, A., Millan, R., Bonnell, J. W., Goldstein, J., Usanova, M., ... Li, X. (2015, July). Observations of coincident EMIC wave activity and duskside energetic electron precipitation on 18-19 January 2013. *Geophys. Res. Lett.*, *42*, 5727-5735. doi: 10.1002/2015GL065245

Blum, L. W., Li, X., & Denton, M. (2015, May). Rapid MeV electron precipitation as observed by SAMPEX/HILT during high-speed stream-driven storms. *J. Geophys. Res.*, *120*, 3783-3794. doi: 10.1002/2014JA020633

Bortnik, J., & Thorne, R. M. (2007, March). The dual role of ELF/VLF chorus waves in the acceleration and precipitation of radiation belt electrons. *Journal of Atmospheric and Solar-Terrestrial Physics*, *69*, 378-386. doi: 10.1016/j.jastp.2006.05.030

Bortnik, J., Thorne, R. M., & Inan, U. S. (2008, November). Nonlinear interaction of energetic electrons with large amplitude chorus. *Geophys. Res. Lett.*, *35*, 21102. doi: 10.1029/2008GL035500

Bortnik, J., Thorne, R. M., Meredith, N. P., & Santolik, O. (2007, August). Ray tracing of penetrating chorus and its implications for the radiation belts. *Geophys. Res. Lett.*, *34*, L15109. doi: 10.1029/2007GL030040

Boynton, R. J., Mourenas, D., & Balikhin, M. A. (2016, September). Electron flux dropouts at Geostationary Earth Orbit: Occurrences, magnitudes, and main driving factors. *Journal of Geophysical Research (Space Physics)*, *121*, 8448-8461. doi: 10.1002/2016JA022916

Boynton, R. J., Mourenas, D., & Balikhin, M. A. (2017, November). Electron Flux Dropouts at $L \sim 4.2$ From Global Positioning System Satellites: Occurrences, Magnitudes, and Main Driving Factors. *Journal of Geophysical Research (Space Physics)*, *122*, 11. doi: 10.1002/2017JA024523

Breneman, A. W., Crew, A., Sample, J., Klumpar, D., Johnson, A., Agapitov, O., ... Kletzing, C. A. (2017, November). Observations Directly Linking Relativistic Electron Microbursts to Whistler Mode Chorus: Van Allen Probes and FIREBIRD II. *Geophys. Res. Lett.*, *44*(22), 11,265-11,272. doi: 10.1002/2017GL075001

Breuillard, H., Zaliznyak, Y., Krasnoselskikh, V., Agapitov, O., Artemyev, A., & Rolland, G. (2012). Chorus wave-normal statistics in the Earth's radiation belts from ray tracing technique. *Ann. Geophys.*, *30*, 1223-1233. doi: 10.5194/angeo-30-1223-2012

Büchner, J., & Zelenyi, L. M. (1989, September). Regular and chaotic charged

particle motion in magnetotaillike field reversals. I - Basic theory of trapped motion. *J. Geophys. Res.*, *94*, 11821-11842. doi: 10.1029/JA094iA09p11821

Bunch, N. L., Spasojevic, M., Shprits, Y. Y., Gu, X., & Foust, F. (2013, April). The spectral extent of chorus in the off-equatorial magnetosphere. *J. Geophys. Res.*, *118*, 1700-1705. doi: 10.1029/2012JA018182

Capannolo, L., Li, W., Ma, Q., Chen, L., Shen, X. C., Spence, H. E., ... Redmon, R. J. (2019, November). Direct Observation of Subrelativistic Electron Precipitation Potentially Driven by EMIC Waves. *Geophys. Res. Lett.*, *46*(22), 12,711-12,721. doi: 10.1029/2019GL084202

Capannolo, L., Li, W., Ma, Q., Qin, M., Shen, X. C., Angelopoulos, V., ... Hanzelka, M. (2023). Electron precipitation observed by elfin using proton precipitation as a proxy for electromagnetic ion cyclotron (emic) waves. *Geophysical Research Letters*. doi: https://doi.org/10.1029/2023GL103519

Chen, L., Thorne, R. M., Li, W., & Bortnik, J. (2013, March). Modeling the wave normal distribution of chorus waves. *J. Geophys. Res.*, *118*, 1074-1088. doi: 10.1029/2012JA018343

Chen, L., Zhang, X.-J., Artemyev, A., Angelopoulos, V., Tsai, E., Wilkins, C., & Horne, R. B. (2022, March). Ducted Chorus Waves Cause Sub-Relativistic and Relativistic Electron Microbursts. *Geophys. Res. Lett.*, *49*(5), e97559. doi: 10.1029/2021GL097559

Chen, L., Zhang, X.-J., Artemyev, A., Zheng, L., Xia, Z., Breneman, A. W., & Horne, R. B. (2021, October). Electron microbursts induced by nonducted chorus waves. *Frontiers in Astronomy and Space Sciences*, *8*, 163. doi: 10.3389/fspas.2021.745927

Chen, R., Gao, X., Lu, Q., & Wang, S. (2019, November). Unraveling the Correlation Between Chorus Wave and Electron Beam-Like Distribution in the Earth's Magnetosphere. *Geophys. Res. Lett.*, *46*(21), 11,671-11,678. doi: 10.1029/2019GL085108

Demekhov, A. G., Trakhtengerts, V. Y., Rycroft, M. J., & Nunn, D. (2006, December). Electron acceleration in the magnetosphere by whistler-mode waves of varying frequency. *Geomagnetism and Aeronomy*, *46*, 711-716. doi: 10.1134/S0016793206060053

Drozdov, A. Y., Shprits, Y. Y., Usanova, M. E., Aseev, N. A., Kellerman, A. C., & Zhu, H. (2017, August). EMIC wave parameterization in the long-term VERB code simulation. *J. Geophys. Res.*, *122*, 8488-8501. doi: 10.1002/2017JA024389

Fu, X., Cowee, M. M., Friedel, R. H., Funsten, H. O., Gary, S. P., Hospodarsky, G. B., ... Winske, D. (2014, October). Whistler anisotropy instabilities as the source of banded chorus: Van Allen Probes observations and particle-in-cell simulations. *Journal of Geophysical Research (Space Physics)*, *119*, 8288-8298. doi: 10.1002/2014JA020364

Gabrielse, C., Angelopoulos, V., Runov, A., & Turner, D. L. (2014, April). Statistical characteristics of particle injections throughout the equatorial magnetotail. *J. Geophys. Res.*, *119*, 2512-2535. doi: 10.1002/2013JA019638

Gan, L., Artemyev, A., Li, W., Zhang, X.-J., Ma, Q., Mourenas, D., ... Wilkins, C. (2023). Bursty energetic electron precipitation by high-order resonance with very-oblique whistler-mode waves. *Geophys. Res. Lett.*. doi: 10.1029/2022GL101920

Gan, L., Li, W., Ma, Q., Artemyev, A. V., & Albert, J. M. (2022). Dependence of nonlinear effects on whistler-mode wave bandwidth and amplitude: A perspective from diffusion coefficients. *J. Geophys. Res.*, *127*, e2021JA030063. doi: 10.1029/2021JA030063

Gendrin, R. (1961, August). Le guidage des whistlers par le champ magnetique. *Planetary Space Science*, *5*, 274. doi: 10.1016/0032-0633(61)90096-4

Glauert, S. A., & Horne, R. B. (2005, April). Calculation of pitch angle and energy

diffusion coefficients with the PADIE code. *J. Geophys. Res.*, *110*, 4206. doi: 10.1029/2004JA010851

Grach, V. S., Artemyev, A. V., Demekhov, A. G., Zhang, X.-J., Bortnik, J., Angelopoulos, V., ... Roberts, O. W. (2022, September). Relativistic Electron Precipitation by EMIC Waves: Importance of Nonlinear Resonant Effects. *Geophys. Res. Lett.*, *49*(17), e99994. doi: 10.1029/2022GL099994

Hanzelka, M., & Santolík, O. (2019, June). Effects of Ducting on Whistler Mode Chorus or Exohiss in the Outer Radiation Belt. *Geophys. Res. Lett.*, *46*(11), 5735-5745. doi: 10.1029/2019GL083115

Hanzelka, M., & Santolík, O. (2022, December). Effects of Field-Aligned Cold Plasma Density Filaments on the Fine Structure of Chorus. *Geophys. Res. Lett.*, *49*(24), e2022GL101654. doi: 10.1029/2022GL101654

Horne, R. B., Glauert, S. A., Meredith, N. P., Boscher, D., Maget, V., Heynderickx, D., & Pitchford, D. (2013, April). Space weather impacts on satellites and forecasting the Earth's electron radiation belts with SPACECAST. *Space Weather*, *11*, 169-186. doi: 10.1002/swe.20023

Hosseini, P., Agapitov, O., Harid, V., & Gołkowski, M. (2021, March). Evidence of Small Scale Plasma Irregularity Effects on Whistler Mode Chorus Propagation. *Geophys. Res. Lett.*, *48*(5), e92850. doi: 10.1029/2021GL092850

Hsieh, Y.-K., & Omura, Y. (2017, January). Nonlinear dynamics of electrons interacting with oblique whistler mode chorus in the magnetosphere. *J. Geophys. Res.*, *122*, 675-694. doi: 10.1002/2016JA023255

Imhof, W. L., Reagan, J. B., & Gaines, E. E. (1977, November). Fine-scale spatial structure in the pitch angle distributions of energetic particles near the midnight trapping boundary. *J. Geophys. Res.*, *82*, 5215-5221. doi: 10.1029/JA082i032p05215

Jun, C. W., Yue, C., Bortnik, J., Lyons, L. R., Nishimura, Y., & Kletzing, C. (2019, Mar). EMIC Wave Properties Associated With and Without Injections in The Inner Magnetosphere. *Journal of Geophysical Research (Space Physics)*, *124*(3), 2029-2045. doi: 10.1029/2018JA026279

Kang, N., & Bortnik, J. (2022, March). Structure of Energy Precipitation Induced by Superbolt-Lightning Generated Whistler Waves. *Geophys. Res. Lett.*, *49*(5), e2022GL097770. doi: 10.1029/2022GL097770

Kang, N., Bortnik, J., Zhang, X., Claudepierre, S., & Shi, X. (2022, December). Relativistic Microburst Scale Size Induced by a Single Point-Source Chorus Element. *Geophys. Res. Lett.*, *49*(23), e2022GL100841. doi: 10.1029/2022GL100841

Katoh, Y., Omura, Y., & Summers, D. (2008, November). Rapid energization of radiation belt electrons by nonlinear wave trapping. *Annales Geophysicae*, *26*, 3451-3456. doi: 10.5194/angeo-26-3451-2008

Ke, Y., Chen, L., Gao, X., Lu, Q., Wang, X., Chen, R., ... Wang, S. (2021, April). Whistler Mode Waves Trapped by Density Irregularities in the Earth's Magnetosphere. *Geophys. Res. Lett.*, *48*(7), e92305. doi: 10.1029/2020GL092305

Ke, Y., Gao, X., Lu, Q., Wang, X., Chen, R., Chen, H., & Wang, S. (2022, February). Deformation of Electron Distributions Due to Landau Trapping by the Whistler-Mode Wave. *Geophys. Res. Lett.*, *49*(3), e96428. doi: 10.1029/2021GL096428

Ke, Y., Gao, X., Lu, Q., Wang, X., & Wang, S. (2017). Generation of rising-tone chorus in a two-dimensional mirror field by using the general curvilinear pic code. *J. Geophys. Res.*. Retrieved from `http://dx.doi.org/10.1002/2017JA024178` doi: 10.1002/2017JA024178

Kennel, C. F., & Engelmann, F. (1966, November). Velocity Space Diffusion from Weak Plasma Turbulence in a Magnetic Field. *Physics of Fluids*, *9*, 2377-2388. doi: 10.1063/1.1761629

Kennel, C. F., & Petschek, H. E. (1966, January). Limit on Stably Trapped Particle

Fluxes. *J. Geophys. Res.*, *71*, 1-28.

Khazanov, G. V., Glocer, A., & Himwich, E. W. (2014, Jan). Magnetosphere-ionosphere energy interchange in the electron diffuse aurora. *Journal of Geophysical Research (Space Physics)*, *119*(1), 171-184. doi: 10.1002/2013JA019325

Khazanov, G. V., Robinson, R. M., Zesta, E., Sibeck, D. G., Chu, M., & Grubbs, G. A. (2018, July). Impact of Precipitating Electrons and Magnetosphere-Ionosphere Coupling Processes on Ionospheric Conductance. *Space Weather*, *16*(7), 829-837. doi: 10.1029/2018SW001837

Kim, H., Schiller, Q., Engebretson, M. J., Noh, S., Kuzichev, I., Lanzerotti, L. J., ... Fromm, T. (2021, February). Observations of Particle Loss due to Injection Associated Electromagnetic Ion Cyclotron Waves. *Journal of Geophysical Research (Space Physics)*, *126*(2), e28503. doi: 10.1029/2020JA028503

Kitahara, M., & Katoh, Y. (2019, Jul). Anomalous Trapping of Low Pitch Angle Electrons by Coherent Whistler Mode Waves. *J. Geophys. Res.*, *124*(7), 5568-5583. doi: 10.1029/2019JA026493

Kong, Z., Gao, X., Chen, H., Lu, Q., Chen, R., Ke, Y., & Wang, S. (2021, November). The Correlation Between Whistler Mode Waves and Electron Beam-Like Distribution: Test Particle Simulations and THEMIS Observations. *Journal of Geophysical Research (Space Physics)*, *126*(11), e29834. doi: 10.1029/2021JA029834

Lam, M. M., Horne, R. B., Meredith, N. P., Glauert, S. A., Moffat-Griffin, T., & Green, J. C. (2010). Origin of energetic electron precipitation¿ 30 kev into the atmosphere. *Journal of Geophysical Research: Space Physics*, *115*(A4).

Li, W., & Hudson, M. K. (2019, Nov). Earth's Van Allen Radiation Belts: From Discovery to the Van Allen Probes Era. *Journal of Geophysical Research (Space Physics)*, *124*(11), 8319-8351. doi: 10.1029/2018JA025940

Li, W., Mourenas, D., Artemyev, A. V., Bortnik, J., Thorne, R. M., Kletzing, C. A., ... Spence, H. E. (2016, September). Unraveling the excitation mechanisms of highly oblique lower band chorus waves. *Geophys. Res. Lett.*, *43*, 8867-8875. doi: 10.1002/2016GL070386

Li, W., Ni, B., Thorne, R. M., Bortnik, J., Green, J. C., Kletzing, C. A., ... Hospodarsky, G. B. (2013, September). Constructing the global distribution of chorus wave intensity using measurements of electrons by the POES satellites and waves by the Van Allen Probes. *Geophys. Res. Lett.*, *40*, 4526-4532. doi: 10.1002/grl.50920

Li, W., Santolik, O., Bortnik, J., Thorne, R. M., Kletzing, C. A., Kurth, W. S., & Hospodarsky, G. B. (2016, May). New chorus wave properties near the equator from Van Allen Probes wave observations. *Geophys. Res. Lett.*, *43*, 4725-4735. doi: 10.1002/2016GL068780

Li, W., Thorne, R. M., Bortnik, J., Nishimura, Y., Angelopoulos, V., Chen, L., ... Bonnell, J. W. (2010, December). Global distributions of suprathermal electrons observed on THEMIS and potential mechanisms for access into the plasmasphere. *J. Geophys. Res.*, *115*, 0. doi: 10.1029/2010JA015687

Li, W., Thorne, R. M., Ma, Q., Ni, B., Bortnik, J., Baker, D. N., ... Claudepierre, S. G. (2014, June). Radiation belt electron acceleration by chorus waves during the 17 March 2013 storm. *J. Geophys. Res.*, *119*, 4681-4693. doi: 10.1002/2014JA019945

Li, W., Thorne, R. M., Nishimura, Y., Bortnik, J., Angelopoulos, V., McFadden, J. P., ... Auster, U. (2010, June). THEMIS analysis of observed equatorial electron distributions responsible for the chorus excitation. *J. Geophys. Res.*, *115*. doi: 10.1029/2009JA014845

Lorentzen, K. R., Blake, J. B., Inan, U. S., & Bortnik, J. (2001, April). Observations of relativistic electron microbursts in association with VLF chorus. *J. Geophys. Res.*, *106*(A4), 6017-6028. doi: 10.1029/2000JA003018

Lyons, L. R., Thorne, R. M., & Kennel, C. F. (1972). Pitch-angle diffusion of radiation belt electrons within the plasmasphere. *J. Geophys. Res.*, *77*, 3455-3474. doi: 10.1029/JA077i019p03455

Ma, Q., Artemyev, A. V., Mourenas, D., Li, W., Thorne, R. M., Kletzing, C. A., ... Wygant, J. (2017, December). Very Oblique Whistler Mode Propagation in the Radiation Belts: Effects of Hot Plasma and Landau Damping. *Geophys. Res. Lett.*, *44*(24), 12,057-12,066. doi: 10.1002/2017GL075892

Ma, Q., Gu, W., Claudepierre, S. G., Li, W., Bortnik, J., Hua, M., & Shen, X. C. (2022, June). Electron Scattering by Very-Low-Frequency and Low-Frequency Waves From Ground Transmitters in the Earth's Inner Radiation Belt and Slot Region. *Journal of Geophysical Research (Space Physics)*, *127*(6), e30349. doi: 10.1029/2022JA030349

Ma, Q., Li, W., Bortnik, J., Thorne, R. M., Chu, X., Ozeke, L. G., ... Claudepierre, S. G. (2018, March). Quantitative Evaluation of Radial Diffusion and Local Acceleration Processes During GEM Challenge Events. *Journal of Geophysical Research (Space Physics)*, *123*(3), 1938-1952. doi: 10.1002/2017JA025114

Ma, Q., Li, W., Thorne, R. M., Ni, B., Kletzing, C. A., Kurth, W. S., ... Angelopoulos, V. (2015, February). Modeling inward diffusion and slow decay of energetic electrons in the Earth's outer radiation belt. *Geophys. Res. Lett.*, *42*, 987-995. doi: 10.1002/2014GL062977

Ma, Q., Ni, B., Tao, X., & Thorne, R. M. (2012, April). Evolution of the plasma sheet electron pitch angle distribution by whistler-mode chorus waves in non-dipole magnetic fields. *Annales Geophysicae*, *30*, 751-760. doi: 10.5194/angeo-30-751-2012

Malaspina, D. M., Ukhorskiy, A., Chu, X., & Wygant, J. (2018, April). A Census of Plasma Waves and Structures Associated With an Injection Front in the Inner Magnetosphere. *J. Geophys. Res.*, *123*, 2566-2587. doi: 10.1002/2017JA025005

Maxworth, A. S., & Golkowski, M. (2017). Magnetospheric whistler mode ray tracing in a warm background plasma with finite electron and ion temperature. *J. Geophys. Res.*, *122*(7), 7323–7335. Retrieved from `http://dx.doi.org/10.1002/2016JA023546` doi: 10.1002/2016JA023546

Meredith, N. P., Horne, R. B., & Anderson, R. R. (2001, July). Substorm dependence of chorus amplitudes: Implications for the acceleration of electrons to relativistic energies. *J. Geophys. Res.*, *106*, 13165-13178. doi: 10.1029/2000JA900156

Meredith, N. P., Horne, R. B., Shen, X.-C., Li, W., & Bortnik, J. (2020). Global model of whistler mode chorus in the near-equatorial region ($|\lambda_m| < 18°$). *Geophys. Res. Lett.*, *47*, e2020GL087311. doi: 10.1029/2020GL087311

Meredith, N. P., Horne, R. B., Sicard-Piet, A., Boscher, D., Yearby, K. H., Li, W., & Thorne, R. M. (2012, October). Global model of lower band and upper band chorus from multiple satellite observations. *J. Geophys. Res.*, *117*, 10225. doi: 10.1029/2012JA017978

Meredith, N. P., Horne, R. B., Thorne, R. M., & Anderson, R. R. (2003, August). Favored regions for chorus-driven electron acceleration to relativistic energies in the Earth's outer radiation belt. *Geophys. Res. Lett.*, *30*(16), 160000-1. doi: 10.1029/2003GL017698

Millan, R. M., & Baker, D. N. (2012, November). Acceleration of Particles to High Energies in Earth's Radiation Belts. *Space Sci. Rev.*, *173*, 103-131. doi: 10.1007/s11214-012-9941-x

Millan, R. M., & Thorne, R. M. (2007, March). Review of radiation belt relativistic electron losses. *Journal of Atmospheric and Solar-Terrestrial Physics*, *69*, 362-377. doi: 10.1016/j.jastp.2006.06.019

Min, K., Liu, K., & Li, W. (2014, July). Signatures of electron Landau resonant interactions with chorus waves from THEMIS observations. *J. Geophys. Res.*,

119, 5551-5560. doi: 10.1002/2014JA019903

Mourenas, D., Artemyev, A. V., Agapitov, O. V., & Krasnoselskikh, V. (2014, April). Consequences of geomagnetic activity on energization and loss of radiation belt electrons by oblique chorus waves. *J. Geophys. Res.*, *119*, 2775-2796. doi: 10.1002/2013JA019674

Mourenas, D., Artemyev, A. V., Agapitov, O. V., Krasnoselskikh, V., & Li, W. (2014, December). Approximate analytical solutions for the trapped electron distribution due to quasi-linear diffusion by whistler mode waves. *J. Geophys. Res.*, *119*, 9962-9977. doi: 10.1002/2014JA020443

Mourenas, D., Artemyev, A. V., Agapitov, O. V., Krasnoselskikh, V., & Mozer, F. S. (2015). Very oblique whistler generation by low-energy electron streams. *J. Geophys. Res.*, *120*, 3665–3683. doi: 10.1002/2015JA021135

Mourenas, D., Artemyev, A. V., Ripoll, J.-F., Agapitov, O. V., & Krasnoselskikh, V. V. (2012). Timescales for electron quasi-linear diffusion by parallel and oblique lower-band Chorus waves. *J. Geophys. Res.*, *117*, A06234. doi: 10.1029/2012JA017717

Mourenas, D., Artemyev, A. V., Zhang, X. J., & Angelopoulos, V. (2022, November). Extreme Energy Spectra of Relativistic Electron Flux in the Outer Radiation Belt. *Journal of Geophysical Research (Space Physics)*, *127*(11), e2022JA031038. doi: 10.1029/2022JA031038

Mourenas, D., Artemyev, A. V., Zhang, X. J., & Angelopoulos, V. (2023, August). Upper Limit on Outer Radiation Belt Electron Flux Based on Dynamical Equilibrium. *Journal of Geophysical Research (Space Physics)*, *128*(8), e2023JA031676. doi: 10.1029/2023JA031676

Mourenas, D., Artemyev, A. V., Zhang, X. J., Angelopoulos, V., Tsai, E., & Wilkins, C. (2021, November). Electron Lifetimes and Diffusion Rates Inferred From ELFIN Measurements at Low Altitude: First Results. *Journal of Geophysical Research (Space Physics)*, *126*(11), e29757. doi: 10.1029/2021JA029757

Mourenas, D., & Ripoll, J.-F. (2012). Analytical estimates of quasi-linear diffusion coefficients and electron lifetimes in the inner radiation belt. *J. Geophys. Res.*, *117*, A01204. doi: 10.1029/2011JA016985

Mourenas, D., Zhang, X. J., Nunn, D., Artemyev, A. V., Angelopoulos, V., Tsai, E., & Wilkins, C. (2022, May). Short Chorus Wave Packets: Generation Within Chorus Elements, Statistics, and Consequences on Energetic Electron Precipitation. *Journal of Geophysical Research (Space Physics)*, *127*(5), e30310. doi: 10.1029/2022JA030310

Mozer, F. S., Agapitov, O., Artemyev, A., Drake, J. F., Krasnoselskikh, V., Lejosne, S., & Vasko, I. (2015). Time domain structures: What and where they are, what they do, and how they are made. *Geophys. Res. Lett.*, *42*, 3627-3638. doi: 10.1002/2015GL063946

Ni, B., Li, W., Thorne, R. M., Bortnik, J., Green, J. C., Kletzing, C. A., ... Soria-Santacruz Pich, M. (2014, July). A novel technique to construct the global distribution of whistler mode chorus wave intensity using low-altitude POES electron data. *J. Geophys. Res.*, *119*, 5685-5699. doi: 10.1002/2014JA019935

Ni, B., Thorne, R. M., Meredith, N. P., Shprits, Y. Y., & Horne, R. B. (2011, October). Diffuse auroral scattering by whistler mode chorus waves: Dependence on wave normal angle distribution. *J. Geophys. Res.*, *116*, 10207. doi: 10.1029/2011JA016517

Ni, B., Thorne, R. M., Shprits, Y. Y., & Bortnik, J. (2008, June). Resonant scattering of plasma sheet electrons by whistler-mode chorus: Contribution to diffuse auroral precipitation. *Geophys. Res. Lett.*, *35*, 11106. doi: 10.1029/2008GL034032

O'Brien, T. P., Looper, M. D., & Blake, J. B. (2004, February). Quantification of relativistic electron microburst losses during the GEM storms. *Geophys. Res.*

Lett., *31*(4), L04802. doi: 10.1029/2003GL018621

O'Brien, T. P., & Moldwin, M. B. (2003, February). Empirical plasmapause models from magnetic indices. *Geophys. Res. Lett.*, *30*, 1152. doi: 10.1029/2002GL016007

Olifer, L., Mann, I. R., Boyd, A. J., Ozeke, L. G., & Choi, D. (2018, May). On the Role of Last Closed Drift Shell Dynamics in Driving Fast Losses and Van Allen Radiation Belt Extinction. *J. Geophys. Res.*, *123*, 3692-3703. doi: 10.1029/2018JA025190

Omura, Y., Furuya, N., & Summers, D. (2007, June). Relativistic turning acceleration of resonant electrons by coherent whistler mode waves in a dipole magnetic field. *J. Geophys. Res.*, *112*, 6236. doi: 10.1029/2006JA012243

Omura, Y., Miyashita, Y., Yoshikawa, M., Summers, D., Hikishima, M., Ebihara, Y., & Kubota, Y. (2015, November). Formation process of relativistic electron flux through interaction with chorus emissions in the Earth's inner magnetosphere. *J. Geophys. Res.*, *120*, 9545-9562. doi: 10.1002/2015JA021563

Orlova, K. G., & Shprits, Y. Y. (2011, September). On the bounce-averaging of scattering rates and the calculation of bounce period. *Physics of Plasmas*, *18*(9), 092904. doi: 10.1063/1.3638137

Rackauckas, C., & Nie, Q. (2017). Differentialequations.jl–a performant and feature-rich ecosystem for solving differential equations in julia. *Journal of Open Research Software*, *5*(1).

Runov, A., Angelopoulos, V., Gabrielse, C., Liu, J., Turner, D. L., & Zhou, X.-Z. (2015, June). Average thermodynamic and spectral properties of plasma in and around dipolarizing flux bundles. *J. Geophys. Res.*, *120*, 4369-4383. doi: 10.1002/2015JA021166

Sauer, K., Baumgaerte, K., & Sydora, R. D. (2020). Gap formation around $\omega_e/2$ and generation of low-band whistler waves by landau-resonant electrons in the magnetosphere: Predictions from dispersion theory. *Earth and Planetary Physics*, *4*, 138. Retrieved from `http://eppcgs.xml-journal.net//article/id/3c6a82bf-66b3-436e-94ce-bc744f2e3c29` doi: 10.26464/epp2020020

Sergeev, V. A., Sazhina, E. M., Tsyganenko, N. A., Lundblad, J. A., & Soraas, F. (1983, October). Pitch-angle scattering of energetic protons in the magnetotail current sheet as the dominant source of their isotropic precipitation into the nightside ionosphere. *Planetary Space Science*, *31*, 1147-1155. doi: 10.1016/0032-0633(83)90103-4

Sheeley, B. W., Moldwin, M. B., Rassoul, H. K., & Anderson, R. R. (2001, November). An empirical plasmasphere and trough density model: CRRES observations. *J. Geophys. Res.*, *106*, 25631-25642. doi: 10.1029/2000JA000286

Shen, X.-C., Li, W., Capannolo, L., Ma, Q., Qin, M., Artemyev, A. V., ... Huang, S. (2023, April). Modulation of Energetic Electron Precipitation Driven by Three Types of Whistler Mode Waves. *Geophys. Res. Lett.*, *50*(8), e2022GL101682. doi: 10.1029/2022GL101682

Shen, Y., Chen, L., Zhang, X.-J., Artemyev, A., Angelopoulos, V., Cully, C. M., ... Horne, R. B. (2021, December). Conjugate Observation of Magnetospheric Chorus Propagating to the Ionosphere by Ducting. *Geophys. Res. Lett.*, *48*(23), e95933. doi: 10.1029/2021GL095933

Shklyar, D. R. (2021, February). A Theory of Interaction Between Relativistic Electrons and Magnetospherically Reflected Whistlers. *Journal of Geophysical Research (Space Physics)*, *126*(2), e28799. doi: 10.1029/2020JA028799

Shklyar, D. R., & Matsumoto, H. (2009, April). Oblique Whistler-Mode Waves in the Inhomogeneous Magnetospheric Plasma: Resonant Interactions with Energetic Charged Particles. *Surveys in Geophysics*, *30*, 55-104. doi: 10.1007/s10712-009-9061-7

Shprits, Y. Y., & Ni, B. (2009, November). Dependence of the quasi-linear scattering rates on the wave normal distribution of chorus waves. *J. Geophys. Res.*,

114, 11205. doi: 10.1029/2009JA014223

Shprits, Y. Y., Subbotin, D. A., Meredith, N. P., & Elkington, S. R. (2008, November). Review of modeling of losses and sources of relativistic electrons in the outer radiation belt II: Local acceleration and loss. *Journal of Atmospheric and Solar-Terrestrial Physics*, *70*, 1694-1713. doi: 10.1016/j.jastp.2008.06.014

Shprits, Y. Y., Thorne, R. M., Friedel, R., Reeves, G. D., Fennell, J., Baker, D. N., & Kanekal, S. G. (2006, November). Outward radial diffusion driven by losses at magnetopause. *J. Geophys. Res.*, *111*, 11214. doi: 10.1029/2006JA011657

Shumko, M., Turner, D. L., O'Brien, T. P., Claudepierre, S. G., Sample, J., Hartley, D. P., ... Mitchell, D. G. (2018, August). Evidence of Microbursts Observed Near the Equatorial Plane in the Outer Van Allen Radiation Belt. *Geophys. Res. Lett.*, *45*(16), 8044-8053. doi: 10.1029/2018GL078451

Stix, T. H. (1962). *The Theory of Plasma Waves.*

Summers, D., Ma, C., Meredith, N. P., Horne, R. B., Thorne, R. M., & Anderson, R. R. (2004, January). Modeling outer-zone relativistic electron response to whistler-mode chorus activity during substorms. *Journal of Atmospheric and Solar-Terrestrial Physics*, *66*, 133-146. doi: 10.1016/j.jastp.2003.09.013

Summers, D., & Ni, B. (2008, July). Effects of latitudinal distributions of particle density and wave power on cyclotron resonant diffusion rates of radiation belt electrons. *Earth, Planets, and Space*, *60*, 763-771.

Summers, D., Ni, B., & Meredith, N. P. (2007, April). Timescales for radiation belt electron acceleration and loss due to resonant wave-particle interactions: 1. Theory. *J. Geophys. Res.*, *112*, 4206. doi: 10.1029/2006JA011801

Tao, X., Bortnik, J., Albert, J. M., & Thorne, R. M. (2012, October). Comparison of bounce-averaged quasi-linear diffusion coefficients for parallel propagating whistler mode waves with test particle simulations. *J. Geophys. Res.*, *117*, 10205. doi: 10.1029/2012JA017931

Tao, X., Thorne, R. M., Li, W., Ni, B., Meredith, N. P., & Horne, R. B. (2011, April). Evolution of electron pitch angle distributions following injection from the plasma sheet. *J. Geophys. Res.*, *116*, A04229. doi: 10.1029/2010JA016245

Thorne, R. M. (1980, March). The importance of energetic particle precipitation on the chemical composition of the middle atmosphere. *Pure and Applied Geophysics*, *118*(1), 128-151. doi: 10.1007/BF01586448

Thorne, R. M. (2010, November). Radiation belt dynamics: The importance of wave-particle interactions. *Geophys. Res. Lett.*, *372*, 22107. doi: 10.1029/2010GL044990

Thorne, R. M., Li, W., Ni, B., Ma, Q., Bortnik, J., Chen, L., ... Kanekal, S. G. (2013, December). Rapid local acceleration of relativistic radiation-belt electrons by magnetospheric chorus. *Nature*, *504*, 411-414. doi: 10.1038/nature12889

Thorne, R. M., O'Brien, T. P., Shprits, Y. Y., Summers, D., & Horne, R. B. (2005, September). Timescale for MeV electron microburst loss during geomagnetic storms. *J. Geophys. Res.*, *110*, 9202. doi: 10.1029/2004JA010882

Tsai, E. (2023, June). *ethantsai/nlwhistlers:jgr2023.* Zenodo. Retrieved from `https://doi.org/10.5281/zenodo.8083874` (Software) doi: 10.5281/zenodo.8083874

Tsai, E., Artemyev, A., Angelopoulos, V., & Zhang, X.-J. (2023, August). Investigating Whistler-Mode Wave Intensity Along Field Lines Using Electron Precipitation Measurements. *Journal of Geophysical Research (Space Physics)*, *128*(8), e2023JA031578. doi: 10.1029/2023JA031578

Tsai, E., Artemyev, A., Zhang, X.-J., & Angelopoulos, V. (2022, May). Relativistic Electron Precipitation Driven by Nonlinear Resonance With Whistler-Mode Waves. *Journal of Geophysical Research (Space Physics)*, *127*(5), e30338. doi: 10.1029/2022JA030338

Tsyganenko, N. A. (1989, January). A magnetospheric magnetic field model with a warped tail current sheet. *Planetary Space Science*, *37*, 5-20. doi: 10.1016/0032-0633(89)90066-4

Turner, D. L., Angelopoulos, V., Li, W., Bortnik, J., Ni, B., Ma, Q., ... Rodriguez, J. V. (2014, March). Competing source and loss mechanisms due to wave-particle interactions in Earth's outer radiation belt during the 30 September to 3 October 2012 geomagnetic storm. *J. Geophys. Res.*, *119*, 1960-1979. doi: 10.1002/2014JA019770

Turunen, E., Kero, A., Verronen, P. T., Miyoshi, Y., Oyama, S.-I., & Saito, S. (2016). Mesospheric ozone destruction by high-energy electron precipitation associated with pulsating aurora. *Journal of Geophysical Research: Atmospheres*, *121*(19), 11–852.

Vainchtein, D., Zhang, X. J., Artemyev, A. V., Mourenas, D., Angelopoulos, V., & Thorne, R. M. (2018, October). Evolution of Electron Distribution Driven by Nonlinear Resonances With Intense Field-Aligned Chorus Waves. *Journal of Geophysical Research (Space Physics)*, *123*(10), 8149-8169. doi: 10.1029/2018JA025654

Vasko, I. Y., Agapitov, O. V., Mozer, F. S., Artemyev, A. V., Drake, J. F., & Kuzichev, I. V. (2017, January). Electron holes in the outer radiation belt: Characteristics and their role in electron energization. *J. Geophys. Res.*, *122*, 120-135. doi: 10.1002/2016JA023083

Vasko, I. Y., Agapitov, O. V., Mozer, F. S., Bonnell, J. W., Artemyev, A. V., Krasnoselskikh, V. V., ... Hospodarsky, G. (2017, May). Electron-acoustic solitons and double layers in the inner magnetosphere. *Geophys. Res. Lett.*, *44*, 4575-4583. doi: 10.1002/2017GL074026

Verkhoglyadova, O. P., Tsurutani, B. T., & Lakhina, G. S. (2010, September). Properties of obliquely propagating chorus. *Journal of Geophysical Research (Space Physics)*, *115*(1), A00F19. doi: 10.1029/2009JA014809

Walsh, B. M., Hull, A. J., Agapitov, O., Mozer, F. S., & Li, H. (2020). A census of magnetospheric electrons from several ev to 30 kev. *Journal of Geophysical Research: Space Physics*, *125*(5), e2019JA027577. Retrieved from `https://agupubs.onlinelibrary.wiley.com/doi/abs/10.1029/2019JA027577` (e2019JA027577 10.1029/2019JA027577) doi: 10.1029/2019JA027577

Wang, D., & Shprits, Y. Y. (2019, July). On How High-Latitude Chorus Waves Tip the Balance Between Acceleration and Loss of Relativistic Electrons. *Geophys. Res. Lett.*, *46*(14), 7945-7954. doi: 10.1029/2019GL082681

Watt, C. E. J., Degeling, A. W., & Rankin, R. (2013, May). Constructing the frequency and wave normal distribution of whistler-mode wave power. *J. Geophys. Res.*, *118*, 1984-1991. doi: 10.1002/jgra.50231

Wilkins, C., Angelopoulos, V., Runov, A., Artemyev, A., Zhang, X. J., Liu, J., & Tsai, E. (2023, October). Statistical Characteristics of the Electron Isotropy Boundary. *Journal of Geophysical Research (Space Physics)*, *128*(10), e2023JA031774. doi: 10.1029/2023JA031774

Xiang, Z., Tu, W., Ni, B., Henderson, M. G., & Cao, X. (2018, August). A Statistical Survey of Radiation Belt Dropouts Observed by Van Allen Probes. *Geophys. Res. Lett.*, *45*, 8035-8043. doi: 10.1029/2018GL078907

Xu, W., Marshall, R. A., Tyssøy, H. N., & Fang, X. (2020). A generalized method for calculating atmospheric ionization by energetic electron precipitation. *Journal of Geophysical Research: Space Physics*, *125*(11), e2020JA028482.

Yahnin, A. G., Yahnina, T. A., Raita, T., & Manninen, J. (2017, September). Ground pulsation magnetometer observations conjugated with relativistic electron precipitation. *Journal of Geophysical Research (Space Physics)*, *122*(9), 9169-9182. doi: 10.1002/2017JA024249

Yahnin, A. G., Yahnina, T. A., Semenova, N. V., Gvozdevsky, B. B., & Pashin, A. B. (2016, September). Relativistic electron precipitation as seen by NOAA

POES. *Journal of Geophysical Research (Space Physics)*, *121*(9), 8286-8299. doi: 10.1002/2016JA022765

Zhang, X., Angelopoulos, V., Artemyev, A. V., & Liu, J. (2018, September). Whistler and Electron Firehose Instability Control of Electron Distributions in and Around Dipolarizing Flux Bundles. *Geophys. Res. Lett.*, *45*, 9380-9389. doi: 10.1029/2018GL079613

Zhang, X.-J., Angelopoulos, V., Artemyev, A., Mourenas, D., Agapitov, O., Tsai, E., & Wilkins, C. (2023, January). Temporal Scales of Electron Precipitation Driven by Whistler-Mode Waves. *Journal of Geophysical Research (Space Physics)*, *128*(1), e2022JA031087. doi: 10.1029/2022JA031087

Zhang, X.-J., Angelopoulos, V., Mourenas, D., Artemyev, A., Tsai, E., & Wilkins, C. (2022, May). Characteristics of Electron Microburst Precipitation Based on High-Resolution ELFIN Measurements. *Journal of Geophysical Research (Space Physics)*, *127*(5), e30509. doi: 10.1029/2022JA030509

Zhang, X. J., Thorne, R., Artemyev, A., Mourenas, D., Angelopoulos, V., Bortnik, J., ... Hospodarsky, G. B. (2018, July). Properties of Intense Field-Aligned Lower-Band Chorus Waves: Implications for Nonlinear Wave-Particle Interactions. *Journal of Geophysical Research (Space Physics)*, *123*(7), 5379-5393. doi: 10.1029/2018JA025390